



**HAL**  
open science

# Ultrastructural Perspectives on the Biology and Taphonomy of Tonian Microfossils From the Draken Formation, Spitsbergen

Alexandre Fadel, Kevin Lepot, Sylvain Bernard, Ahmed Addad, Armelle Riboulleau, Andrew H. Knoll

► **To cite this version:**

Alexandre Fadel, Kevin Lepot, Sylvain Bernard, Ahmed Addad, Armelle Riboulleau, et al.. Ultrastructural Perspectives on the Biology and Taphonomy of Tonian Microfossils From the Draken Formation, Spitsbergen. *Geobiology*, 2024, 22 (6), 10.1111/gbi.70000 . hal-04817903

**HAL Id: hal-04817903**

**<https://hal.science/hal-04817903v1>**

Submitted on 17 Jan 2025

**HAL** is a multi-disciplinary open access archive for the deposit and dissemination of scientific research documents, whether they are published or not. The documents may come from teaching and research institutions in France or abroad, or from public or private research centers.


L'archive ouverte pluridisciplinaire **HAL**, est destinée au dépôt et à la diffusion de documents scientifiques de niveau recherche, publiés ou non, émanant des établissements d'enseignement et de recherche français ou étrangers, des laboratoires publics ou privés.



Distributed under a Creative Commons Attribution 4.0 International License

ORIGINAL ARTICLE OPEN ACCESS

# Ultrastructural Perspectives on the Biology and Taphonomy of Tonian Microfossils From the Draken Formation, Spitsbergen

Alexandre Fadel<sup>1,2</sup>  | Kevin Lepot<sup>1,3</sup>  | Sylvain Bernard<sup>4</sup> | Ahmed Addad<sup>5</sup> | Armelle Riboulleau<sup>1</sup> | Andrew H. Knoll<sup>6</sup>

<sup>1</sup>Univ. Lille, CNRS, Univ. Littoral Côte d'Opale, IRD, UMR 8187 – LOG – Laboratoire d'Océanologie et de Géosciences, F-59000 Lille, France | <sup>2</sup>Univ. Lille, CNRS, INRAE, Centrale Lille, Univ. Artois, FR 2638 – IMEC – Institut Michel-Eugène Chevreul, F-59000 Lille, France | <sup>3</sup>Institut Universitaire de France (IUF), Paris, France | <sup>4</sup>Institut de Minéralogie, Physique des Matériaux et de Cosmochimie (IMPMC), CNRS UMR 7590, Muséum National d'Histoire Naturelle, Sorbonne Université, Paris, France | <sup>5</sup>Univ. Lille, CNRS, INRAE, Centrale Lille, UMR 8207 – UMET – Unité Matériaux et Transformations, F-59000 Lille, France | <sup>6</sup>Department of Organismic and Evolutionary Biology, Harvard University, Cambridge, Massachusetts, USA

**Correspondence:** Kevin Lepot ([kevin.lepot@univ-lille.fr](mailto:kevin.lepot@univ-lille.fr))

**Received:** 8 December 2023 | **Revised:** 14 July 2024 | **Accepted:** 30 September 2024

**Funding:** This work was supported by the Agence Nationale de la Recherche, European Regional Development Fund, Région Hauts-de-France, Canadian Light Source, Ministère de l'Enseignement supérieur, de la Recherche et de l'Innovation, Diamond Light Source, Métropole Européenne de Lille, and RENATECH Network.

**Keywords:** cell wall | membranes | microfossils | Proterozoic | transmission electron microscopy | ultrastructure

## ABSTRACT

Silicified peritidal carbonates of the Tonian Draken Formation, Spitsbergen, contain highly diverse and well-preserved microfossil assemblages dominated by filamentous microbial mats, but also including diverse benthic and/or allochthonous (possibly planktonic) microorganisms. Here, we characterize eight morphospecies in focused ion beam (FIB) ultrathin sections using transmission electron microscopy (TEM) and X-ray absorption near-edge structure (XANES) spectromicroscopy. Raman and XANES spectroscopies show the highly aromatic molecular structure of preserved organic matter. Despite this apparently poor molecular preservation, nano-quartz crystallization allowed for the preservation of various ultrastructures distinguished in TEM. In some filamentous microfossils (*Siphonophycus*) as well as in all cyanobacterial coccoids, extracellular polysaccharide sheaths appear as bands of dispersed organic nanoparticles. *Synodophycus* microfossils, made up of pluricellular colonies of coccoids, contain organic walls similar to the F-layers of pleurocapsalean cyanobacteria. In some fossils, internal content occurs as particulate organic matter, forming dense networks throughout ghosts of the intracellular space (e.g., in *Salome svalbardensis* filaments), or scarce granules (in some *Chroococcales*). In some chroococcalean microfossils (*Gloeodiniopsis mikros*, and also possibly *Polybessurus*), we find layered internal contents that are more continuous than nanoparticulate bands defining the sheaths, and with a shape that can be contracted, folded, or invaginated. We interpret these internal layers as the remains of cell envelope substructures and/or photosynthetic membranes thickened by additional cellular material. Some *Myxococcoides* show a thick (up to ~0.9 μm) wall ultrastructure displaying organic pillars that is best reconciled with a eukaryotic affinity. Finally, a large spheroid with ruptured wall, of uncertain affinity, displays a bi-layered envelope. Altogether, our nanoscale investigations provide unprecedented insights into the taphonomy and taxonomy of this well-preserved assemblage, which can help to assess the nature of organic microstructures in older rocks.

This is an open access article under the terms of the [Creative Commons Attribution](https://creativecommons.org/licenses/by/4.0/) License, which permits use, distribution and reproduction in any medium, provided the original work is properly cited.

© 2024 The Author(s). *Geobiology* published by John Wiley & Sons Ltd.

## 1 | Introduction

For most of life's history, Earth's biota was predominantly microbial (Knoll, Bergmann, and Strauss 2016; Brocks et al. 2017). Proterozoic rocks preserve a relative abundance and diversity of microfossils, but while some can be assigned to specific cyanobacterial (e.g., Green et al. 1987) or eukaryotic (e.g., Butterfield 2001; Porter, Meisterfeld, and Knoll 2003; Tang et al. 2020) clades, most have simple morphologies that preclude detailed phylogenetic attribution. Proterozoic microfossils also provide an important framework for the interpretation of scarce and less obviously biogenic organic microstructures preserved in Archean rocks. Nevertheless, the biogenic origin of many Archean microstructures continues to be debated (Brasier et al. 2015; Knoll, Bergmann, and Strauss 2016; Lepot 2020; Coutant et al. 2022). Even some of the most abundant morphotypes of Gunflint-type assemblages, considered as reference microfossils of the Paleoproterozoic Era (Javaux and Lepot 2018), have recently been questioned (Lekele Baghekema et al. 2017; Nims et al. 2021). These difficulties underscore the need for nanoscale ultrastructural and chemical investigation to complement microscale morphological description.

TEM was applied to silicified Neoproterozoic microfossils from the Bitter Springs Formation as early as 1976 (Oehler 1976a), although insights from this work ran more toward taphonomy than phylogeny. More recently, TEM imaging of wall ultrastructure has been applied to analyze eukaryotic microfossils preserved in Proterozoic shales (Arouri, Greenwood, and Walter 1999, 2000; Javaux, Knoll, and Walter 2003, 2004; Willman 2009; Agić, Moczyłowska, and Yin 2015). Microscale and nanoscale textural and chemical characterization has also been applied to Neoproterozoic microfossil assemblages preserved in early diagenetic silica (Oehler 1976a, 1977; Oehler et al. 2006; Lemelle et al. 2008; Igisu et al. 2009; Foucher and Westall 2013; Williford et al. 2013; Wacey, Eiloart, and Saunders 2019a). These studies show how difficult it can be to confirm the eukaryotic affinity of some microfossils, underscoring the need for phylogenetic criteria. Recently, wall, sheath and membrane ultrastructures helped distinguish cyanobacteria in ca. 1 Ga and 1.78–1.73 shales (Demoulin, Lara, et al. 2024; Demoulin, Sforza, et al. 2024).

Here, we investigate the ultrastructure, molecular structure and composition of various microfossils preserved in early diagenetic chert of the Neoproterozoic Draken Formation, Spitsbergen (Knoll, Sweet, and Mark 1991). Inferences about organic matter maturity are in turn compared with other Proterozoic assemblages and Archean rocks. For the first time, we investigate the ultrastructure of a large number (15) of microfossils, spanning eight morphospecies, at the nanoscale, together with their mineral matrices. Our nanoscale investigations reveal several nanostructures not clearly discernible by optical microscopy, which in turn are used to constrain the taphonomy and taxonomy of these microfossils.

## 2 | Geological Setting

The studied microfossils come from the Neoproterozoic Draken Formation, exposed in nunataks in northeastern Spitsbergen.

The Draken Formation forms part of a thick (1900 m) carbonate ramp deposited in an actively subsiding rift basin (Harland and Wilson 1956; Wilson 1961; Knoll and Swett 1990; Maloof et al. 2006; Halverson et al. 2018). Radiometric dates on C-isotope excursions that underlie and overlie the Draken Formation constrain its depositional age to be younger than ca. 800 Ma and older than  $739.9 \pm 6.1$  Ma (Strauss et al. 2014; Halverson et al. 2018). Halverson et al. (2018) have correlated an isotopic event near the top of the carbonate succession with strata in northwestern Canada dated at  $752.7 \pm 5.5$  Ma, based on Re-Os systematics (Strauss et al. 2014). An age estimate of  $788 \pm 0.94$  Ma for the base of the Draken Formation based on Bayesian modeling of subsidence history of the Akademikerbreen Group as a whole (Zhang et al. 2023) is broadly consistent with the first appearances of biostratigraphically informative vase-shaped microfossils (VSMS) elsewhere (Martí Mus, Moczyłowska, and Knoll 2020). Although well exposed and well preserved, Draken rocks were affected by Caledonian orogenesis (the Silurian-Devonian Ny Friesland orogeny; Harland and Gayer 1972; Harland et al. 1992; Gee and Page 1994; Lyberis and Manby 1999; Halverson et al. 2007, 2018), but the metamorphic grade of sampled sections remains below greenschist facies.

The Draken Formation is 150–250 m thick, consisting principally of dolomitic intraformational conglomerate interbedded with micrite, grainstone and subordinate microbialites (Knoll, Sweet, and Mark 1991). The middle third of the formation includes relatively abundant oolitic and oncolitic facies, while the upper part contains columnar stromatolites and microbial laminites, with tepee structures associated with thin intraclastic dolomites and dolomicrites (Knoll, Sweet, and Mark 1991). Microfossils are preserved in several Draken lithologies, including both carbonates and shale. However, the best preservation is found in early diagenetic cherts forming black tabular shards in intraformational breccia. Indeed, the best-preserved microfossils occur within a single bed less than a meter thick.

Lithologically, the fossiliferous bed consists of mm-thick, platy clasts floating in a matrix of well sorted fine sand to mud (Figure S1a), termed flake conglomerate by Wilson (1961). Flakes of the conglomerate represent microbial mats that were penecontemporaneously cemented, ripped up and redeposited during storms. The Draken flake conglomerate formed in a lagoon bounded landward by extensive tidal flats and seaward by shallow subtidal stromatolites (Fairchild, Knoll, and Swett 1991; Knoll, Sweet, and Mark 1991). Microfossil assemblages in individual flakes vary from solitary populations of tightly interwoven mat builders to diverse assemblages in which mat dwellers and allochthonous elements (sedimented planktonic and/or transported benthic microorganisms) contribute strongly to taxonomic richness. By analogy to modern mat systems, this is interpreted to indicate that episodic storms ripped up clasts from across a broad intertidal to shallow subtidal gradient, depositing them in the lagoon. Flakes were silicified individually, but several observations indicate that silicification occurred after formation of the conglomerate. Flakes are commonly bent, indicating that they were somewhat flexible at the time of sedimentation; within penecontemporaneous dolomite nodules formed in the sediments, flakes remain unsilicified, indicating that silicification followed precipitation of the dolomite nodules. Chert

boundaries do not always adhere strictly to flake boundaries, again indicating post-depositional silicification (Knoll, Sweet, and Mark 1991). Still, the commonly excellent preservation of microfossils indicates that the chert formed rapidly before extensive decay of the organic mat components (Wilson 1961; Knoll 1982, 2003; Knoll, Sweet, and Mark 1991; Manning-Berg et al. 2019), the specific association with flakes reflecting the nucleation of silica on organic matter in redeposited mat shards (Knoll 1985).

Five biofacies have been recognized in the Draken Formation, interpreted in terms of position along a tidal flat gradient (see table 1 in Fairchild, Knoll, and Swett 1991, or table 9 in Knoll, Sweet, and Mark 1991). The *Melanocytrillium* biofacies named for the VSMs present in this assemblage (Fairchild, Knoll, and Swett 1991; Knoll, Sweet, and Mark 1991) is characteristic of the subtidal, lagoonal environment; in addition to VSMs, it also contains ornamented acritarchs and 10–20  $\mu\text{m}$  spheroids assigned to the form genus *Myxococcoides*. The second biofacies is composed predominantly of densely interwoven filaments of *Siphonophycus septatum*, interpreted as the extracellular sheaths of cyanobacterial mat builders and associated with auxiliary *Scytonema*-like filaments of *S. svalbardensis*. This subfacies, characteristic of lower intertidal or transitional lagoon also contains diverse micro-benthic taxa and common allochthonous *Myxococcoides* (Figure S1b) (Fairchild, Knoll, and Swett 1991; Knoll, Sweet, and Mark 1991). The third biofacies is composed of thin-walled *Siphonophycus inornatum*, the main mat builders of intertidal zone. As in the second biofacies, the mats builders are associated with diverse micro-benthic taxa and common allochthonous *Myxococcoides* spp. (Figure 1a,b, Figure S1d) (Fairchild, Knoll, and Swett 1991; Knoll, Sweet, and Mark 1991). The fourth biofacies is composed of thick-walled *Siphonophycus inornatum*, characteristic of the upper intertidal zone (Figure 1c). This biofacies contains few micro-benthic or allochthonous microfossils (Figure S1c) (Fairchild, Knoll, and Swett 1991; Knoll, Sweet, and Mark 1991). The final biofacies, composed almost entirely of *Siphonophycus kestron* filaments, with additional populations rare or absent, is characteristic of the upper intertidal to supratidal zone (Fairchild, Knoll, and Swett 1991; Knoll, Sweet, and Mark 1991). The samples studied here, labelled P4353-1B, -5A, -6A, and -11A, come from cliffs of the Polarishreen area of northeastern Spitsbergen and correspond to subsamples of the rocks described in Knoll, Sweet, and Mark (1991).

### 3 | Methods

#### 3.1 | Semi-Thin Sections

All observations and analyses were carried out on 400–500  $\mu\text{m}$  thick, polished uncovered semi-thin sections prepared following the procedure developed by Fadel et al. (2020) to minimize organic contaminants.

The advantage of these semi-thin sections is that their preparation and observation do not require that the section be glued onto a slide. In addition, the semi-thin sections were rinsed with organic solvents (acetone, ethanol, followed by HPLC grade

dichloromethane and methanol) to remove labile molecules in zones close to the surface that are open to fluids.

#### 3.2 | Optical Microscopy

Optical petrography and microfossil localization were carried out using an Olympus BX60 microscope and a Nikon Eclipse Ni-E with automatized stage (at LOG, U. Lille) under bright-field transmitted light and reflected light. Photomicrographs from single focal planes were combined into “multiplane images” using a weighted average algorithm (CombineZP software by Alan Hadley, or the EDF function of NIS Elements AR 5.02.00) in order to fully describe each microfossil and microfossil clusters (Bercovici, Hadley, and Villanueva-Amadoz 2009; Lepot 2021). All photomicrographs of microfossils are multiplane images, unless otherwise specified. Images were used to locate microfossils at or near the surface of the semi-thin sections for further analyses, including Raman spectroscopy, scanning electron microscopy (SEM) and transmission electron microscopy (TEM) on the same microfossils.

#### 3.3 | Raman Spectroscopy

Raman spectra of microfossils were obtained using a LabRam HR800UV Raman microspectrometer (Horiba Jobin Yvon) (at LOG, U. Lille). The spectra were acquired with a 532 nm laser focused through an Olympus BX41 microscope with 50 $\times$  objective (long working distance NA = 0.75) during 1–2 min. Spectra were obtained in focus at least 1–2  $\mu\text{m}$  below the surface of thin sections following the recommendations of Beyssac et al. (2003) with a laser power delivered at the sample surface of ca. 30  $\mu\text{W}$  following the recommendations of Jakubek and Fries (2023), thereby preventing irreversible thermal damage. The backscattered Raman signal was collected through a 50  $\mu\text{m}$  confocal pinhole and dispersed by a grating (1800 lines/mm) and analyzed with a front-illuminated CCD detector. Spectra were fitted with the fityk software by Marcin Wojdyr (Wojdyr 2010).

#### 3.4 | SEM and Focused Ion Beam

SEM images were recorded on gold–palladium coated (~20 nm-thick deposit) thin sections using a FEI Quanta 200 SEM (at LOG, U. Lille). The secondary electron images (SE) revealed the topographic features that located targets for the preparation of ultrathin sections of microfossils with focused ion beam (FIB). FIB sections were prepared with a FEI strata Dual-Beam 235 FIB (at IEMN, U. Lille) for Transmitted Electron Microscopy. During the FIB section preparation, the top surface of each region of interest was protected with platinum strip ~25  $\mu\text{m}$  long and ~2  $\mu\text{m}$  thick. Material on each side of the region of interest was removed by a gallium ( $\text{Ga}^+$ ) ion beam (30 kV, 7 nA). Then, FIB sections were lifted out and attached onto a copper TEM grid by depositing platinum at the contact(s) between the section and the grid. The section was thinned to ~150–200 nm using beam with decreasing current (1 nA to 300 and 100 pA) grazing on each side of the section. Milling at low gallium ion currents allowed minimizing common artefacts including local gallium implantation, mixing of components, redeposition of



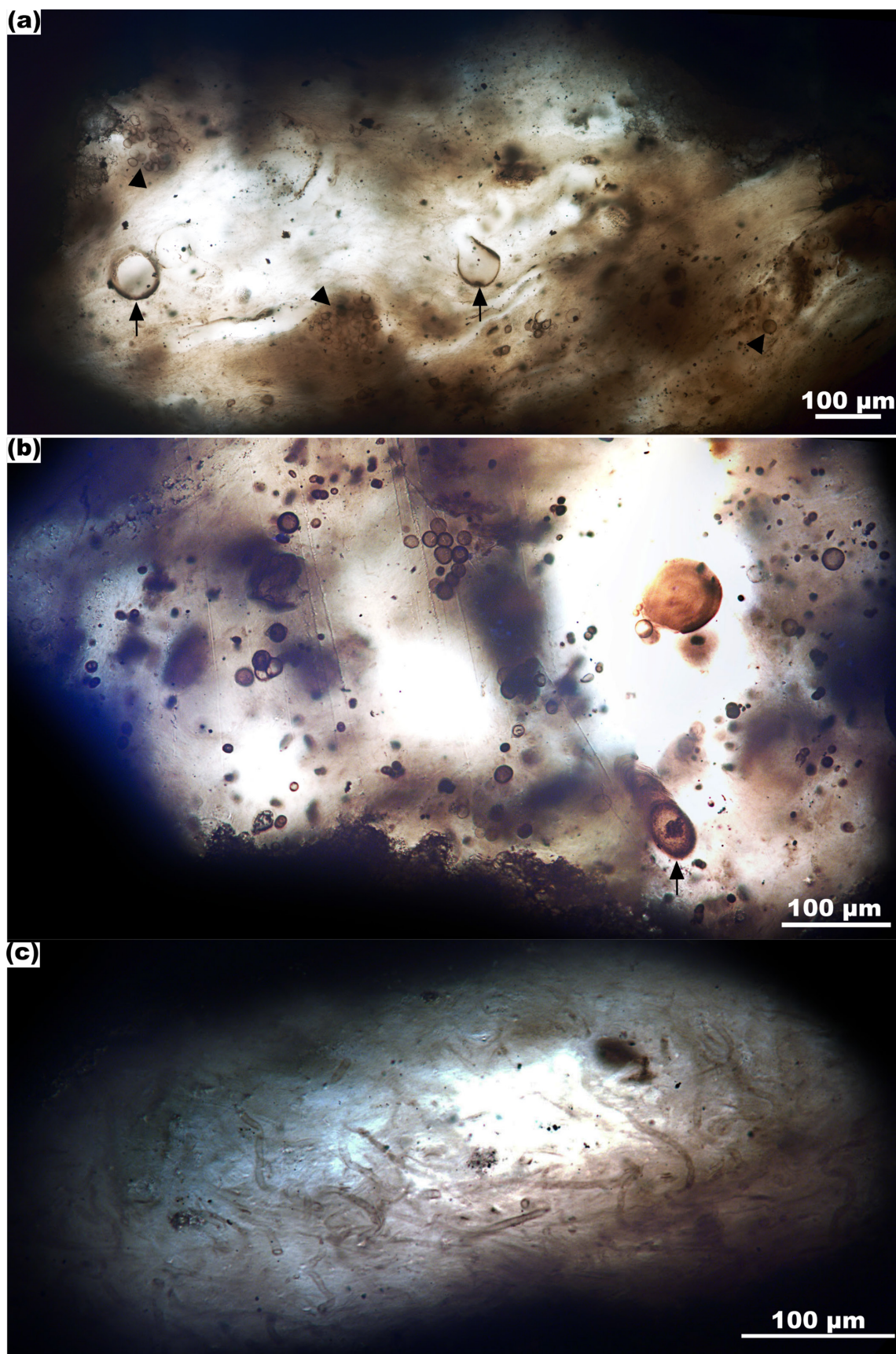


**FIGURE 1** | General view of cherty lenses containing diverse microfossil assemblages. (a) Assemblage of microfossils including scarce large ruptured spheroids (arrows) and various *Myxococcoides* spheroids (arrowheads) from lagoonal setting. (b) Highly diverse cherty lens containing various allochthonous and microbenthic microfossils (arrow: *Polybessurus*). (c) Microbial mats only composed of *Siphonophycus inornatum*. Samples, in a: P4353-1B, b and c: P4353-6A.

the sputtered material on the sample surface and significant changes in the speciation of carbon-based polymers (Bernard et al. 2009; Schiffbauer and Xiao 2009).

### 3.5 | Scanning Transmission Electron Microscopy

TEM analyses were performed on the FIB sections on a FEI TITAN Themis 300 TEM (this work was carried out on the electron microscopy facility of the Advanced Characterization Platform of the Chevreul Institute), operated at 80 and 300 kV. The FIB sections were inserted into the microscope using a cryo-transfer holder (model 914, Gatan) cooled by liquid N<sub>2</sub>. Liquid N<sub>2</sub> was added after 3 h, to allow the recovery of microscope vacuum and avoid formation of frost on the FIB sections. The microscope is equipped with a monochromator and a Cs probe corrector. For high-angle annular dark-field (HAADF) image acquisition in the scanning transmission electron microscopy (STEM) mode, the spot size was #8 (producing a screen current of ~50–90 pA) and the camera length was 91 mm. For dark-field STEM images, the same parameters were used but the camera length was 285 mm. The contrasts in STEM HAADF images are only influenced by the atomic weight of elements, whereas STEM dark-field images are more influenced by diffraction contrasts. In order to highlight the distribution of carbonaceous matter, and distinguish the latter from pores in the FIB section, energy-filtered TEM (EFTEM) elemental maps of carbon were obtained using the three window techniques. The two pre-edge images were recorded at 242.5 and 265.5 eV and the post-edge at 287.5 eV with a windows width of 21 eV. Alignment of the pre- and post-edge images was performed manually. When FIB sections present thickness or diffraction contrast variations, the two window technique was used to reconstruct the EFTEM maps. Elemental distributions were mapped using a Super-X EDXS (energy-dispersive X-ray spectrometry) detector (formed by four SSD detectors integrated to the S-TWIN objective lens), which is sensitive to light-weight elements. This detector allowed us to produce EDXS mappings of the sample in the same horizontal position as that used to record all STEM and EFTEM images. Additional TEM imaging was performed using a FEI Tecnai G2 20 (this work was carried out on the electron microscopy facility of the Advanced Characterization Platform of the Chevreul Institute), operated at 200 kV.

### 3.6 | XANES-STXM

STXM analyses were performed on FIB sections at the Diamond Light Source beamline I08-SXM and the Canadian Light Source (CLS) beamline 10ID-1 (SM). The I08-SXM beamline uses radiation ranging from 250 to 4400 eV, generated by an Apple II type undulator. The X-ray source is optimized to enable studies exploiting linearly or circularly polarized radiation. The intensity of the X-rays transmitted through the sample is directly measured using a photodiode. STXM was used to perform high resolution (~30 nm) spectromicroscopy at the carbon K-edge (energy range 275–295 eV) to image the distribution of organic matter and characterize the carbon chemistry in X-ray absorption near-edge spectroscopy (XANES) spectra. We recorded XANES hyperspectral stacks using a spectral resolution of 0.1 eV between

275 and 295 eV and counting times of 3–5 milliseconds per pixel. XANES stack data were normalized to the absorption of the background. Aromatic carbon maps were obtained by subtraction of X-ray transmission images recorded in mapstacks (using 15 ms/pixel to improve contrasts) at 285.1 eV (aromatics)—280.1 eV (pre-edge absorption ‘baseline’). Preliminary analysis was also performed on one microfossil at the CLS beamline 10-ID1 (Kaznatcheev et al. 2007) (chamber back-filled with He instead of vacuum; PMT detector, inferred flux in the 10<sup>6</sup> photons·cm<sup>-2</sup> order of magnitude, spatial resolution < 25 nm, dwell time ≤ 2 ms). Alignment of images of stacks, extraction of XANES spectra, and aromatic carbon maps were obtained using the aXis2000 software (Hitchcock 2023). Interpretation of XANES signals was based on information available in the literature (e.g., Bernard et al. 2010; Le Guillou et al. 2018).

## 4 | Results and Interpretations

### 4.1 | Microfossil Assemblage

Our study focused on chert flakes displaying a high variety of well-preserved microfossils (Figure 1a,b, Figure S1b–d), interpreted as microbenthic mat dwellers and allochthonous (probably planktonic) microorganisms (Knoll 1982; Knoll, Sweet, and Mark 1991). Variable amounts of mat-building filaments populate the flakes, forming distinct populations of densely interwoven filaments, likely the polysaccharide sheaths of mat-forming cyanobacteria (Figure 1c, Figure S1c,d). The most abundant and diverse microbenthic and allochthonous populations occur in the lowest density mat-building populations, probably because these lower intertidal or marginal subtidal mats trapped and bound carbonate mud (compare cherts in Figure 1a,b vs. c). These well-preserved microfossil assemblages are commonly associated with pyrite crystals (also reported by Foucher and Westall 2013; Lemelle et al. 2008; Gomes et al. 2018). Unicellular and colonial coccoids, associated with the filaments in microbial mats, are highly diverse in the Draken biota (Knoll 1982; Knoll, Sweet, and Mark 1991). Here we focus on six coccoid morphospecies, as well as the dominant type of filaments (*Siphonophycus*), and another rare filamentous morphospecies.

### 4.2 | Structure of the Carbonaceous Material

#### 4.2.1 | Raman Spectra

The excellent morphological preservation of the microfossils as structured carbonaceous remains has been highlighted with Raman mapping by Foucher and Westall (2013). In sample P4353-1B, we analyzed spheroidal microfossils (with either sub-continuous or clotted/granular walls), *Siphonophycus* sheaths (with either dark organic-rich or light organic-lean matrices), as well as clotted organic matter that can form veinlets up to a few hundred micrometers in length (Figure S2a–k, S2w<sub>1–4</sub>). In sample P4353-5A we analyzed various microfossils, veins that cut across multiple chert lenses and/or clasts, and clots/veinlets of smaller (submillimetric), unconstrained distribution (Figure S2l–u). Microfossils of samples P4353-11A and -6A were also analyzed (Figure S2v<sub>1–3</sub>, S2w<sub>1–2</sub>). All



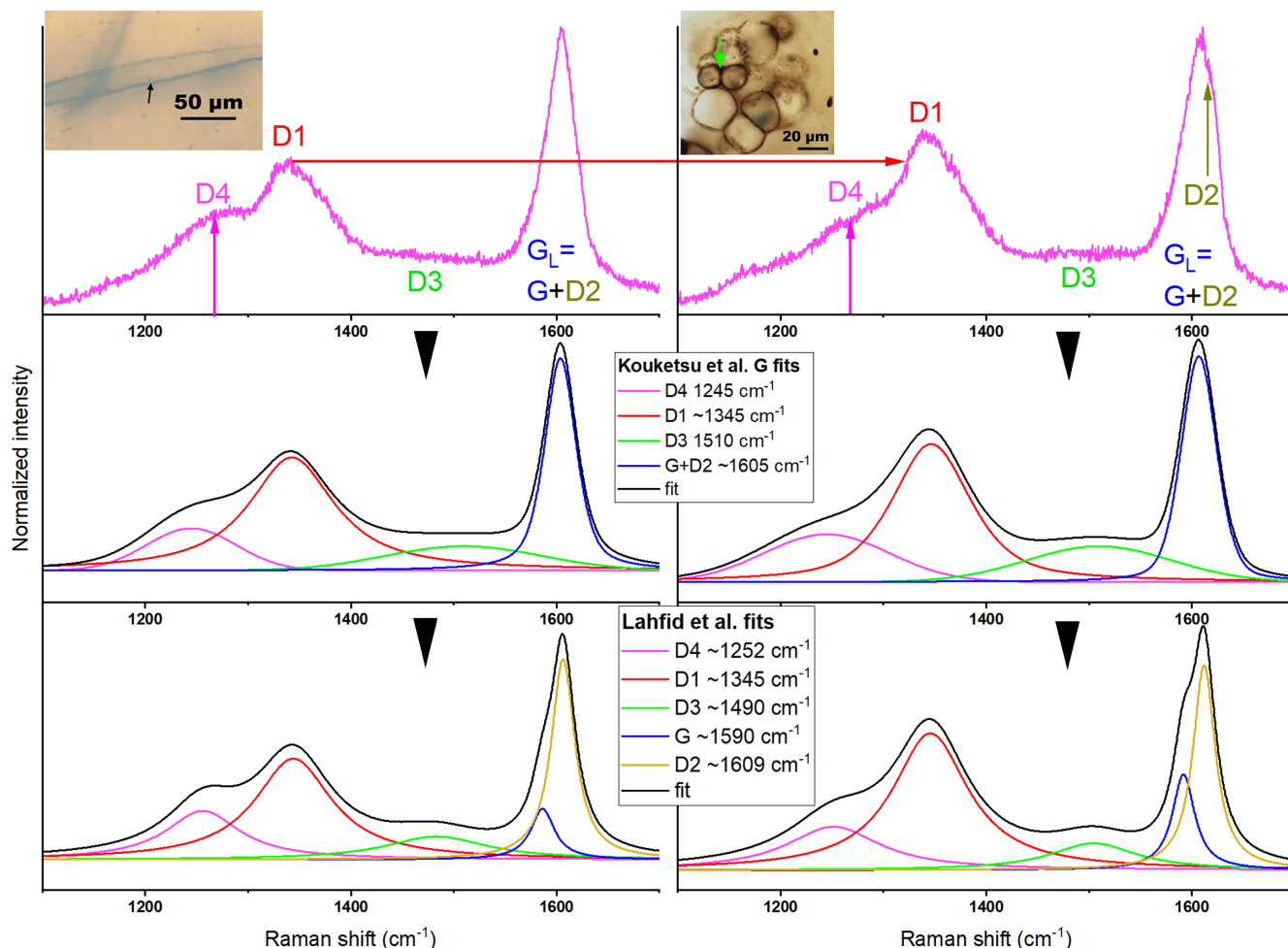


**FIGURE 2** | Raman spectra from a carbonaceous vein (top left) and a microfossil (top right) and their deconvolution using the Kouketsu et al. (2014) G method (central row) and the Lahfid et al. (2010) method (lower row). Arrows highlight the main spectral differences between the two targets for bands D4 (pink arrow, higher in vein), D1 (red arrow, higher in fossils) and D2 (split of  $G_L = G + D2$  doublet forming shoulder at D2: Brown arrow). Sample P4353-5A (locations in Figure S2). The deconvolutions show the functions generated by the fitting procedures, which generate the band parameters shown in Table S1.

spectra display D1 to D4 and G bands between 1000 and 2000  $\text{cm}^{-1}$  typical of kerogen, with small variations in band intensities (Figure 2, Figure S3).

To further evaluate these heterogeneities and to estimate the peak metamorphism temperature of kerogen, we used peak-fitting decompositions. The G method of Kouketsu et al. (2014) that uses pseudo-Voigt functions bands for D1, D2, D3 D4 was utilized, as all  $G_L/D_1$  ratio values of the spectra are higher than 1.5 (Table S1). We also used the method of Lahfid et al. (2010), fitting D1 to D4 and G bands with Lorentz functions. We obtained spectral parameters and peak temperature estimates following the methods of Lahfid et al. (2010), Kouketsu et al. (2014), and that derived by Baludikay et al. (2018) from the methods of Liu et al. (2013) and Barker and Pawlewicz (1994), as listed in Table S1 and compared in Figure S3. The method of Lahfid et al. (2010) is based on the use of 514 nm excitation, whereas the other two methods used 532 nm lasers, which could lead to imprecision in the application of the Lahfid et al. (2010) model to our dataset recorded with 532 nm excitation. The main heterogeneity lies between the microfossils of sample P4353-5A and the associated veins

and clots/veinlets, where the former display relatively higher D1 bands, lower D4/D1 band ratio, and an apparent split of the  $G_L$  ( $G + D2$ ) band forming a D2 shoulder (Figure 2). Microfossils in samples P4353-6A and -11A display Raman parameters similar to those of -5A. All carbonaceous textures in sample P4353-1B display Raman parameters intermediate between those of microfossils in other samples and veins/clots in P4353-5A. While the  $G_L/D_1$  ratio is higher in microfossils of P4353-1B relative to other samples, the D4/D1 height ratio does not vary much between these samples, whereas it is significantly higher in veins of P4353-5A. This highlights the distinct spectral signature of veins in sample P4353-5A.

#### 4.2.2 | OM Geothermometry

Temperature estimates obtained from the D1 band and those obtained from the D2 band (equations 1 and 2 of Kouketsu et al. 2014, respectively, see footnote of Table S1) are inconsistent, probably linked to the unusual height of the D4 band, which influences the fitting of the D1 band. For all OM analyzed in the Draken samples (except the P4353-5A sample vein/veinlets/

clots), we estimate a ca. 266°C burial temperature supplied by “equation 2” of Kouketsu et al. (2014) and very much consistent with estimates from both equations of Lahfid et al. (2010) (Table S1). We note the lower temperatures estimated from the Baludikay et al. (2018) thermometers for burial conditions (218 and 236°C, respectively), as is the case for other geological settings (Baludikay et al. 2018).

#### 4.2.3 | Maturity Interpretations

These Raman data indicate that the OM in all microfossils as well as in veins and clotted textures is over-mature, having entered the metamorphism window. The maturity is well above that of the Paleoproterozoic microfossils from the Gunflint Formation (Alleon et al. 2016b) and of other Proterozoic microfossils studied by Baludikay et al. (2018), Guo et al. (2018) and Nabhan et al. (2021). Based on the smaller D3 and D4 bands of the Draken microfossil Raman spectra, we can also infer that the Draken microfossils are significantly more mature than those of the Bitter Springs Formation (Schopf et al. 2005). The observed kerogen maturity in Draken microfossils is closer to that of kerogen in some Neoproterozoic stromatolites (Lepot et al. 2008), that of the Paleoproterozoic microfossils of the Francevillian FC formation (Lekele Baghekema et al. 2017) and that of microfossils of the Duck Creek Formation (Fadel et al. 2017; this outcrop was originally assigned to the older Turee Creek Group, but has now been shown to be a Duck Creek equivalent by U–Pb zircon dating of an included volcanic ash bed: Wingate et al. 2022). Slightly lower temperatures may be inferred for the vein-OM with the Kouketsu et al. (2014) equation 1 thermometer, that is ca. 272° against ca. 288°C in microfossils (Table S1). In any case, the veins in sample P4353-5A are likely filled with migrated bitumen that has turned into pyrobitumen at such temperatures. Aromatic carbon contents of 92% or more are indicated by <sup>13</sup>C NMR for OM of the Gunflint Formation (Delarue et al. 2016). This suggests that the more mature OM of the Draken Formation may be even more aromatic.

### 4.3 | Composition of the Organic Matter

#### 4.3.1 | X-Ray Spectroscopy Results

The XANES spectrum obtained at the Diamond Light Source from a filamentous microfossil (Figure 3e) only displays aromatic carbon (band #1 in Figure 3e), but does not display the exciton feature at 291.7 eV characteristic of highly graphitic carbon materials (Bernard et al. 2010). A putative microfossil, likely highly degraded, that forms a spindle-like structure with internally reticulated OM and an internal vesicle, but does not display diagnostic cellular ultrastructure (Figure S4), was analyzed at CLS. Its spectrum (Figure 3e, in gray) shows additional weak signals of C=O bonds with a band (#3) at ~287.5 eV indicative of ketone C=O, a band at ~288.5 eV (#4) indicative of carboxylic C=O, and a shoulder at ~286.3 eV (#2) that could be attributed to unsaturated bonds between carbon and sulfur atoms (Bernard et al. 2012). Independent EDX investigations conducted on a 1 μm long kerogen grain from a FIB section revealed a low amount of N and S (Figure S5).

#### 4.3.2 | Interpretation of the Molecular Composition

In the Draken microfossils, organic sulfur was reported by Lemelle et al. (2008). Thus some heteroatoms may be preserved in the Draken microfossils, consistent with the spectrum measured at CLS. The discrepancies between data collected at CLS and Diamond may be due to (i) radiation damage at Diamond, (ii) contamination at CLS or (iii) intrinsic heterogeneities. Radiation damage at Diamond is a plausible explanation, the photon dose at Diamond being higher than at CLS. Still, abundant heteroatomic functional groups have been measured in Proterozoic microfossils (Nabhan et al. 2021) and in a meteorite (Steele et al. 2022) at Diamond, using similar or higher photon doses (Bonneville et al. 2020). In any case, both datasets (Figure 3e) point to a mostly aromatic composition of the Draken microfossils, consistent with Raman spectroscopy. Altogether, the organic material composing the Draken microfossils appears to be more degraded chemically than the organic material composing the 1.88 Ga Gunflint microfossils, which have experienced lower temperature as indicated by Raman spectroscopy (Alleon et al. 2016b). The advanced thermal degradation shown by the highly aromatic composition of the Draken microfossils unfortunately prevents discussing the original chemical nature of the different microfossil morphospecies based on the available spectroscopy.

### 4.4 | *Siphonophycus* Filaments

#### 4.4.1 | Assignment Using Published Criteria

The filaments present in the lower flake conglomerate were interpreted as the remains of cyanobacterial sheaths by Knoll (1982) and Knoll, Sweet, and Mark (1991). These filaments include several species of *Siphonophycus* filaments, which are differentiated on the basis of their cross-sectional diameters (Schopf 1968; Zhang 1981; Knoll 1982); the distinct species, so defined, consistently show different patterns of facies distribution in the Draken Formation and elsewhere (Knoll 1982; Knoll, Sweet, and Mark 1991). The studied filaments occur in mat assemblages with diverse other mat-dwellers or allochthonous microfossils (Knoll, Sweet, and Mark 1991).

#### 4.4.2 | (S)TEM Imaging

We extracted a longitudinal FIB section that intercepted a ~5 μm diameter filament (*S. inornatum*) with a thick central organic thread and another *Siphonophycus* forming an empty sheath (specimens 1a and 1b, respectively, Figure 3a–d, Figure S4e). Multiplane photomicrographs show that specimen 1a, throughout its lengths, displays a dark central thread embedded in more transparent tubular sheath (Figure S4e). We also prepared a transverse FIB section of a filament with only scarce internal organic granules (specimen 2, Figure S6). Central organic threads and granules (Figure 3d, Figure S6e) are nanoporous (pore size <20 nm). The outer limits of filamentous specimens 1a and 1b are defined by thin (<10 to ca. 100 nm) layers of organic matter (Figure 3a–c), which appear sub-continuous to discontinuous within the resolution limit of EFTEM imaging. In contrast, specimen 2 comprises an irregular band (>1 μm large) composed of dispersed nanogranular organic matter (Figure S6). Quartz

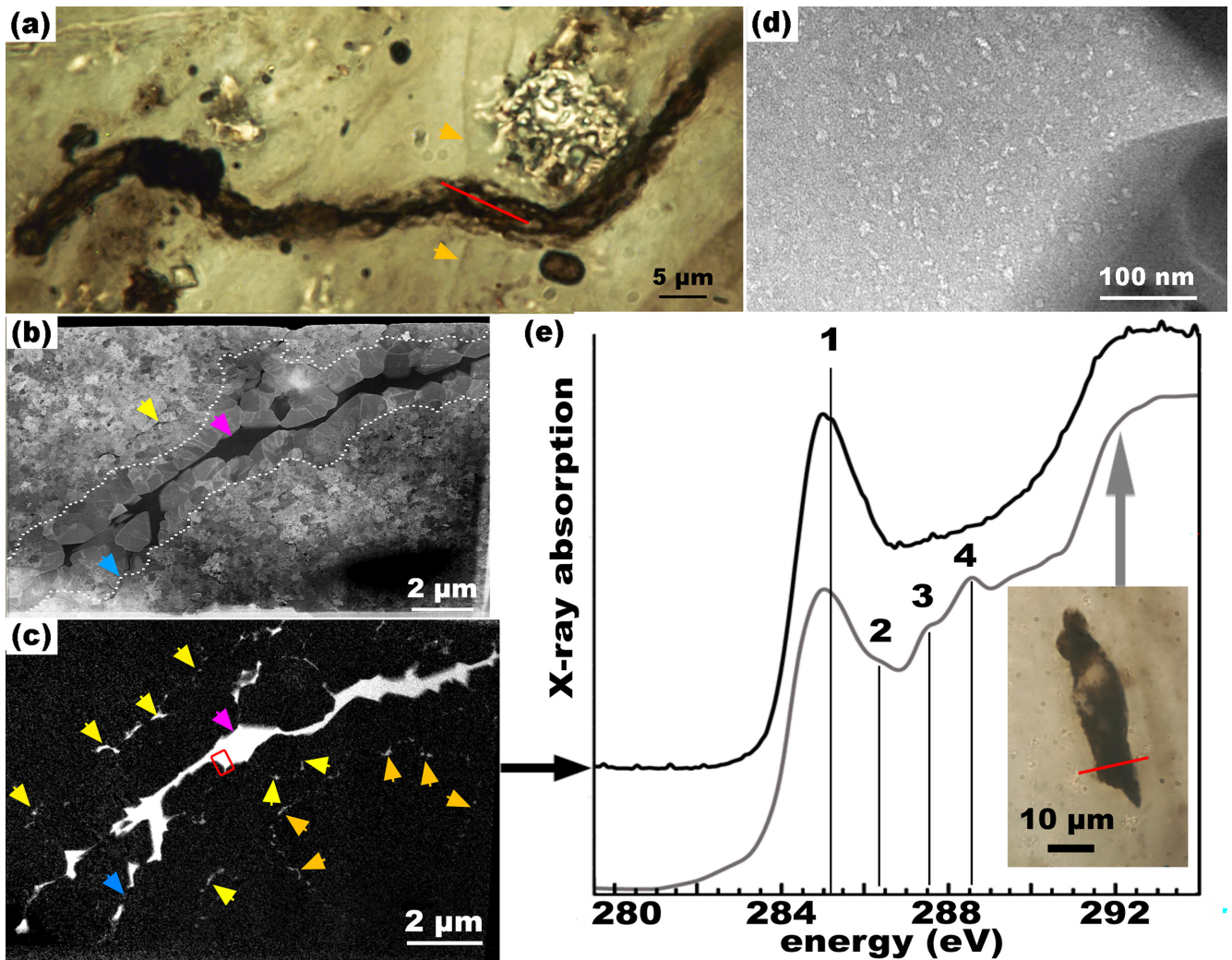


**FIGURE 3** | *Siphonophycus* filaments 1a–1b and unidentified putative microfossil. (a) *Siphonophycus*, multiplane photomicrograph in transmitted light (Red line: FIB section position in filament 1a; orange arrows: Filament 1b passing below 1a). (b) STEM dark-field image of the FIB section. Quartz crystals appear in shades of gray due to variable diffraction contrast. Coarse quartz crystals occur within the filament and are surrounded by nanocrystals; dotted line highlights the interface between two quartz types. (c) EFTEM elemental map of carbon (in white). Arrows: Pink = central thread, yellow/orange = outermost organic layer of filaments 1a/1b, respectively, blue = migration/branching of the central thread at the interface between micro and nano-quartz. (d) Bright-field TEM image of the red-boxed zone in c, showing nanoporosity (white) in the carbonaceous matter (light-gray) of the central thread; adjacent quartz grains appear in black. (e) C K-edge XANES spectra, in black: From the central thread of carbonaceous matter at the pink arrow in b–c, analyzed at Diamond (the spectrum appears shifted by  $-0.3$  eV); in gray: From an unidentified putative microfossil or microfossil fragment (inset, Figure S4a–d), analyzed at the CLS. See main text for peak 1–4 assignment. Samples: P4353-11A and P4353-6A.

nanocrystals ( $\sim 100$ – $200$  nm in diameter, Figure 3b, Figure S6b) occur inside and throughout their outer layer/band and outside of the filaments. Coarser quartz (crystals up to  $\sim 3$   $\mu$ m in diameter) outline the thick central organic thread of specimen 1a (see dotted line in Figure 3b). The internal carbonaceous granule of specimen 2 is surrounded by quartz crystals slightly coarser (up to ca.  $500$  nm in length) than those filling the rest of the fossil (Figure S6). The full section of specimen 1b is filled by nano-quartz (Figure 3b).

#### 4.4.3 | Interpretations

These differences of quartz mineralogy, organic matter texture, and the close spatial distribution of these microfossils (distance between the different filamentous microfossils is less

than  $500$   $\mu$ m) suggest that the taphonomy of microfossils can be highly variable at the microscopic scale. The quartz size distribution in filament specimens 1a and 2 can be explained by initial impregnation of the outer envelope (and surrounding matrix) by fine-grained silica while cellular contents remained preserved, followed by the infilling of the microfossil interior after post-mortem transformation of cellular contents (Konhauser et al. 2004; Lynne et al. 2005). Such secondary infilling by coarser quartz has indeed been documented in Campbell et al. (2015). The homogenous distribution of nanoquartz in specimen 1b suggests complete cell lysis may have occurred before a single step impregnation of the filaments.

The thin outer layer observed in filament specimens 1a and 1b may be explained by preservation of a thin extracellular sheath (e.g., figure 3 in Gonzalez-Esquer et al. 2016). Alternatively, it



may represent the preservation of the outer cell envelope layer, which is found in some filamentous cyanobacteria as a tubular (longitudinal) layer that surrounds multiple cells of the trichome and that is absent from their septa and cross-walls (Hoiczky and Baumeister 1995). This serrated outer external envelope layer can be 15–35 nm thick, commonly 40–50 nm including overlying fibrillar layer (Hoiczky and Baumeister 1995), and appears to reach over 100 nm in *Oscillatoria sancta* (online resource 3 in Gonzalez-Esquer et al. 2016).

In contrast, the broad (> 1 μm) band of dispersed nanoparticle OM in specimen 2 (Figure S6) is best reconciled with the impregnation of porous polysaccharide network by nano-quartz during silicification of sheath (Gong et al. 2020). The porosity may have been generated by the lysis of an amorphous part of the sheath, preserving only the fibrillar substructure (Daft and Stewart 1973). Remains of the later may represent the source of the nanoparticulate OM.

The structure of filament specimen 1a includes an outer layer and a central thread, which has also been observed in a microfossil of the older Gunflint Formation (figure 3e in Javaux and Lepot 2018). Three explanations for the formation of this structure can be proposed. The canonical explanation is that the outermost thin layer (or more discontinuous band) of organic matter represents the remnant of the sheath, while the dense and irregular inner organic thread (or scarce internal granules in specimen 2) corresponds to collapsed and diagenetically polymerized cell material. Such a pattern of post-mortem decay has been observed in modern microbial mats (see, for example, Gomes et al. 2020, and references therein). Dense to variably porous organic matter observed within dinoflagellate microfossils has similarly been interpreted as the result of post-mortem polymerization of lipids from the cells and from ambient fluids (Versteegh et al. 2004). Second, the inner thread could correspond to collapsed cell ± sheath material as observed in modern taphonomic experiments (Bartley 1996). We argue that this central thread is unlikely to have formed by collapsed *Siphonophycus* sheath material only, as the empty sheaths in specimens 1b and 2 (Figure 3c, Figure S6) do not appear to contain sufficient organic material to account for such a thick thread. Third, the central organic thread could represent bitumen that could have migrated in the open porosity left after decay of the cells, as suggested for the Gunflint Formation microfossils (Rasmussen, Muhling, and Fischer 2021, see also Sasaki et al. 2022). The nanoporous structure of the central thread in specimen 1a is consistent with pyrobitumen, i.e., the solid product of bitumen secondary cracking (Bernard and Horsfield 2014). In this scenario, the outermost thin layer could represent organic matter that migrated further away from the central thread (Knoll, Strother, and Rossi 1988). Indeed, some organic matter appears to have migrated from the central thread between the micrometric quartz grains to rest at the interface between micro- and nano-quartz (blue arrows in Figure 3). However, the outermost thin layer is fully surrounded by nanoquartz and there is no clear evidence of organic matter migration in the nanoquartz area between the microquartz and this outer layer (e.g., between the yellow and pink arrows in Figure 3). Alternatively, the nano-porosity may represent devolatilization during FIB preparation of small islands of solid bitumen

trapped in the kerogen, although this appears unlikely in such mature rocks (Katz and Arango 2018).

Our observations support the interpretation that the central nanoporous threads/granules represent diagenetically polymerized cell material with possible migration of organic material/bitumen, whereas the thin outer layers represent the remnants of polysaccharide sheaths or outer envelope layers. This hypothesis also explains the carbon isotope ratio heterogeneities between sheaths/walls and internal granules observed in some Neoproterozoic microfossils (Williford et al. 2013). Interestingly, a similar Raman signature is observed for *Siphonophycus* sheaths in dark, organic-rich zones and light, organic-poor zones, and a distinct Raman signature is found for microfossils and adjacent carbonaceous veins (Figure 2, Figures S2, S3). This contrasts with the heterogeneous bitumen staining of hollow filamentous microfossils observed close to bitumen veins in some hydrothermally-reworked chert clasts of the Red Dog deposit (Rasmussen and Muhling 2019). Thus, bitumen staining alone cannot explain all the organic matter present in these Draken microfossils, and some original kerogen is likely preserved.

Cellular material was likely still preserved after peripheral encrustation of the microorganism as observed for modern bacteria, which are first encrusted externally and/or within the polysaccharide sheath by metastable opal before crystallization of quartz (Westall, Boni, and Guerzoni 1995; Jones, Renaut, and Rosen 1998; Phoenix, Adams, and Konhauser 2000; Konhauser et al. 2004; Lalonde et al. 2005). The contacts between the coarser quartz crystals and the central organic thread do not show the “sawtooth-like” pattern described by Wacey et al. (2012) and Lekele Baghekema et al. (2017), which has been interpreted by the latter authors as the effect of microquartz formation by recrystallization of nanoquartz. Thus, it appears that the morphology of the quartz microcrystals associated with the central thread was not controlled by the texture of the internal organic matter. Rather, the geopolymer forming the central thread likely polymerized and/or migrated locally between the microquartz crystals. Thus, the living and/or decaying microorganisms probably lowered the rate of quartz crystal growth as observed in fossilization experiments (e.g., Alleon et al. 2016a) during the initial encrustation of the inner and outer surfaces of the sheath material. Late silicification then occurred in local pore space after cell lysis, ultimately leading to the formation of coarser quartz in specimen 1a (Figure 3).

## 4.5 | *Salome svalbardensis* Filament

### 4.5.1 | Assignment

*Salome svalbardensis* is a rare type of filament composed of a trichome—a chain of disc-shaped cells ~2 μm long and ~6–15 μm wide—within a multilayered sheath. The sheath structure includes an inner sheath with a cross section of 8–16 μm. This inner sheath is surrounded by up to eight outer sheath layers with cross sections ranging between 23 and 65 μm. Sheath layers are diffuse and can be difficult to recognize due to the low abundance of organic matter (Figure 4a) and the presence

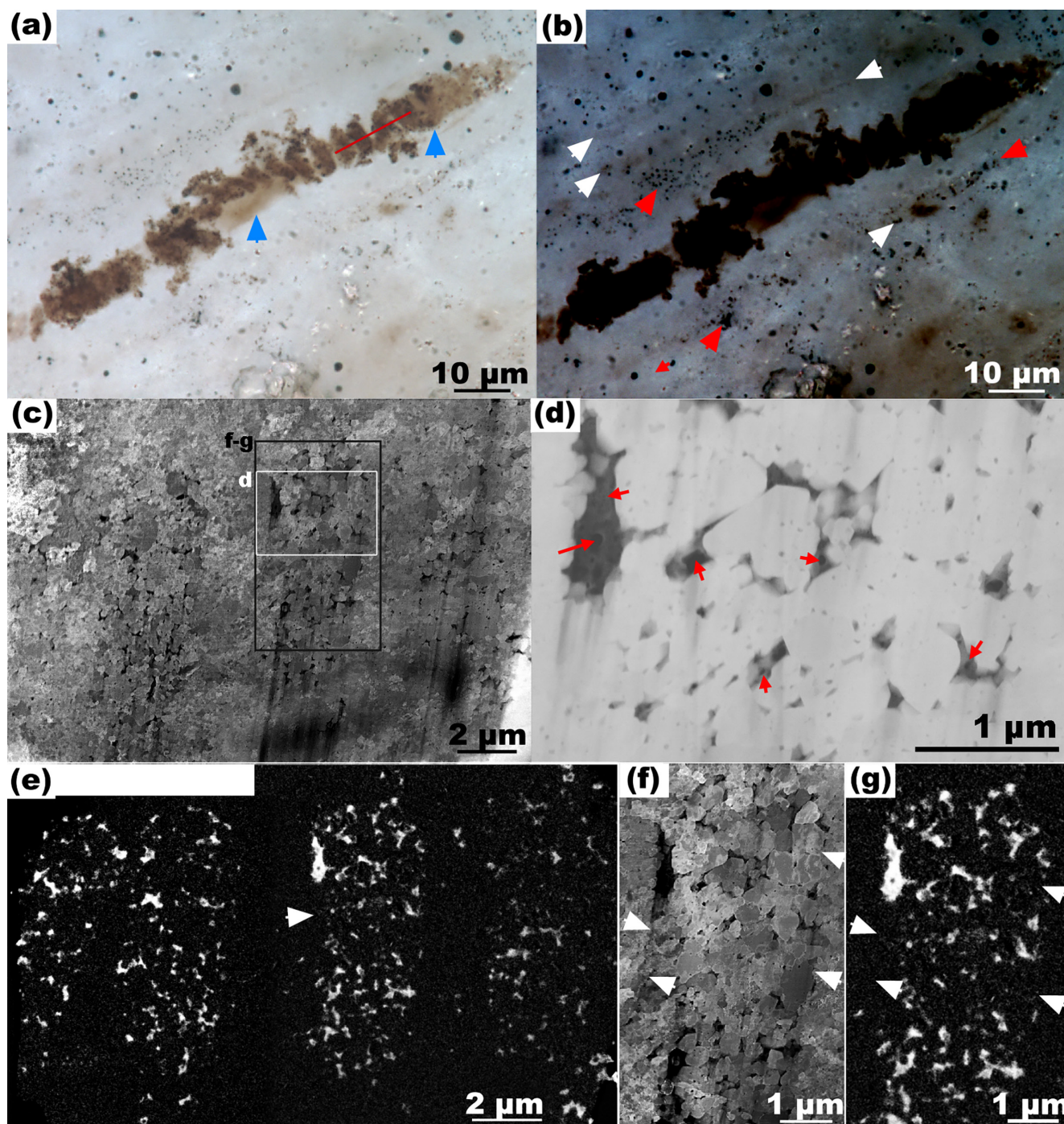


**FIGURE 4** | *Salome svalbardensis* microfossil. (a) Photomicrograph in transmitted light (Red line: FIB section position; arrows: Internal organic material). (b) High contrast photomicrograph of the microfossil. Here white arrows outline the multiple organic sheath layers, and red arrows outline local enrichments in nano-pyrites. (c) Dark-field STEM image of the FIB section showing quartz nano-crystals (in various shades of gray). (d) HAADF STEM image of white-boxed zone in c showing porosity (black) in OM (dark-gray) within the quartz matrix (white). (e) EFTEM elemental map of carbon (in white) showing the distribution of organic matter within disc-shaped cells. White arrow: Cell limit devoid of carbon. Sub-vertical lines in c–d and f are an artifact of the FIB preparation process (Liu et al. 2016). (f) Zoom on the black box in c. (g) EFTEM map of carbon in f. The white arrows in f–g indicate the position of sharp contacts between quartz crystals inside and outside the cell that are devoid of carbon. Sample P4353-1B.

of nanopyrites (Figure 4b). In terms of morphology, this fossil population is closely similar to species of *Scytonema* found in modern microbial mat communities (e.g., Gomes et al. 2020) and is almost certainly cyanobacterial (Knoll 1982). Individual

disc-shaped cells are heterogeneously preserved along the filament, and are often replaced by large tubes and clots of organic matter (Figure 4a). In this context, it is difficult to determine if the diffuse tubular brownish material surrounding preserved



cells (arrows in Figure 4a) represents an inner sheath material or degraded cellular material.

#### 4.5.2 | (S)TEM Imaging

The FIB section shows that the cells comprise 200–600 nm large organic particles that are apparently randomly distributed (Figure 4d–g). These organic particles are nanoporous, with some pores larger than 100 nm (Figure 4d). A low density of organic nanoparticles occurs between the well-defined cells. Interestingly, these nanoparticles are less abundant (absent?) in the sheath region above the cells in Figure 4d,e. The quartz between the cells and within the sheath structure comprises nanocrystals of ~100–300 nm in diameter. The quartz crystals within the disc-shaped cells are slightly larger, reaching up to 1 μm in diameter. Interestingly, some quartz crystals at the inner border of the cell structures are elongated at the contact with the former cell envelope and can define the border of the cell structure where carbon is absent (white arrows in Figure 4e–g).

#### 4.5.3 | Interpretations

The small size of quartz grains in cells and sheaths suggests that early silicification was pervasive and might have prevented (in *Salome*) the coarse aggregation of organic matter in the shape of thick central threads and grains as observed in *Siphonophycus* (Figure 3, Figure S6). The sharp contact of cell-filling quartz grains (some elongated) with nano-grains from the sheath suggests that multiple crystallization episodes occurred in this *Salome* microfossil (Figure 4c,f). The sheath was likely silicified first and a second episode silicified the cells (Figure 4a). It is commonly viewed that polysaccharide sheath and wall ultrastructures are more resistant to decomposition than cellular membrane and intracellular contents (Chalansonnet et al. 1988; Bartley 1996; Jones, Renaut, and Rosen 2001; Lepot et al. 2014; Campbell et al. 2015; Gomes et al. 2020). Nevertheless, some cyanobacterial cell contents (in particular, thylakoid membranes) and cytoplasmic membranes may survive longer than peptidoglycan wall layer in some early *post mortem* stages (Zheng et al. 2013). Here, no part of the cell envelopes is preserved. The random distribution of organic matter within the cells (Figure 4d–g) likely results from diagenetic polymerization, possibly including intracellular materials and/or additional ambient molecules or bitumen. Secondary cracking of bitumen is consistent with the nanoporous texture of the organic matter. The texture of inner organic grains is similar to that observed in a *Paleolyngbya* (cyanobacterial) microfossil studied by demineralization and TEM (Oehler 1976a), although the latter displayed crosswalls, unlike this *Salome* microfossil. Furthermore, the submicrometric quartz present within the cell appears to form locally a cast of the wall without preservation of organic matter (Figure 4e–g, arrows). This suggests that the silicification of the sheaths and cells prevented the extensive aggregation of organic particles and complete loss of ultrastructure. The outer cell wall was likely encrusted first by silica due to preferential hydrogen bond formation between the hydroxyl groups of silicic acid and cell wall molecules (Orange et al. 2009). After the lysis of the cells, the wall was obliterated and aggregation

of the cellular organic matter inside the cell structure was likely associated with the second cell-infilling silicification episode. This *Salome* microfossil suggests the preservation of cellular contents of filamentous cyanobacteria during rapid silicification processes, as observed in the Tonian Bitter Springs Formation (Schopf 1968), the early Mesoproterozoic Gaoyuzhuang Formation (Zhang 1981) and elsewhere.

## 4.6 | *Gloeodiniopsis mikros* Coccoids

### 4.6.1 | Assignment

*Gloeodiniopsis lamellosa*, first described from the ca. 800 Ma Bitter Springs Formations (Schopf 1968), consists of large inner-wall structures organized in monads, dyads or tetrads (~12.5 μm in diameter) surrounded by four to six thick, concentric outer layers (Schopf 1968). More generally, spheroids with multilamellated envelopes have conventionally been ascribed to *Gloeodiniopsis*, but the state of preservation of inner and outer structures can be variable (Knoll and Golubic 1979). The Draken material contains several *Gloeodiniopsis* morphospecies, including *G. mikros*, the smallest morphospecies of this genus (Knoll 1982). This microfossil, abundant in *S. inornatum* mat shards, is composed of spheroidal smooth-walled inner vesicles (~3 μm in diameter) of optically dense organic matter, interpreted as cell remnants, enclosed in an external envelope (~8 μm in diameter, Figure 5a) interpreted as a polysaccharide capsule (Knoll 1982; Knoll, Sweet, and Mark 1991). External envelopes contain one, two or four vesicles following a simple division pattern. The cyanobacterial affinity of *G. mikros* has been inferred by Knoll (1982) based on similarity of size, morphology and division pattern with modern Chroococaceae, especially the genus *Chroococcus* (i.e., *C. minutus*: Geitler 1932) and *Gloeocapsa*. While the specimens observed are composed of single layered sheath, the assignment of the microfossils present in the Figure 5a and Figure S7 is based on the size, the wall texture of inner vesicles and the organization of similar microfossils in dyads/tetrads in the shards where microfossils are hosted. Moreover, the specimens studied have similar size and morphologies with the *G. mikros* population reported in previous studies (Knoll, Sweet, and Mark 1991).

### 4.6.2 | (S)TEM Imaging

FIB sections of *G. mikros* were extracted from two cells of a dyad (specimens 1a, Figure 5 and 1b, Figure S7d–f) and from a monad (specimen 2, Figure S7a–c). Quartz crystals within or outside specimen 1a are ~200–500 nm in diameter (Figure 5b). In all three specimens, the outer layer comprises a peripheral band of organic matter, ~0.5–1 μm in thickness composed of dispersed organic grains <100 nm in diameter (Figure 5c,d, red arrows, Figure S7), and local reticulated texture (Figure S7e). A broad organic-poor zone is observed between this peripheral band and the inner vesicles of all specimens (green arrow in Figure 5).

The organic matter within the inner vesicles of *G. mikros* is not randomly dispersed (as seen in *S. svalbardensis*) but formed thinner layers (arrowheads in Figure 5, Figure S7). In specimen 1a, a

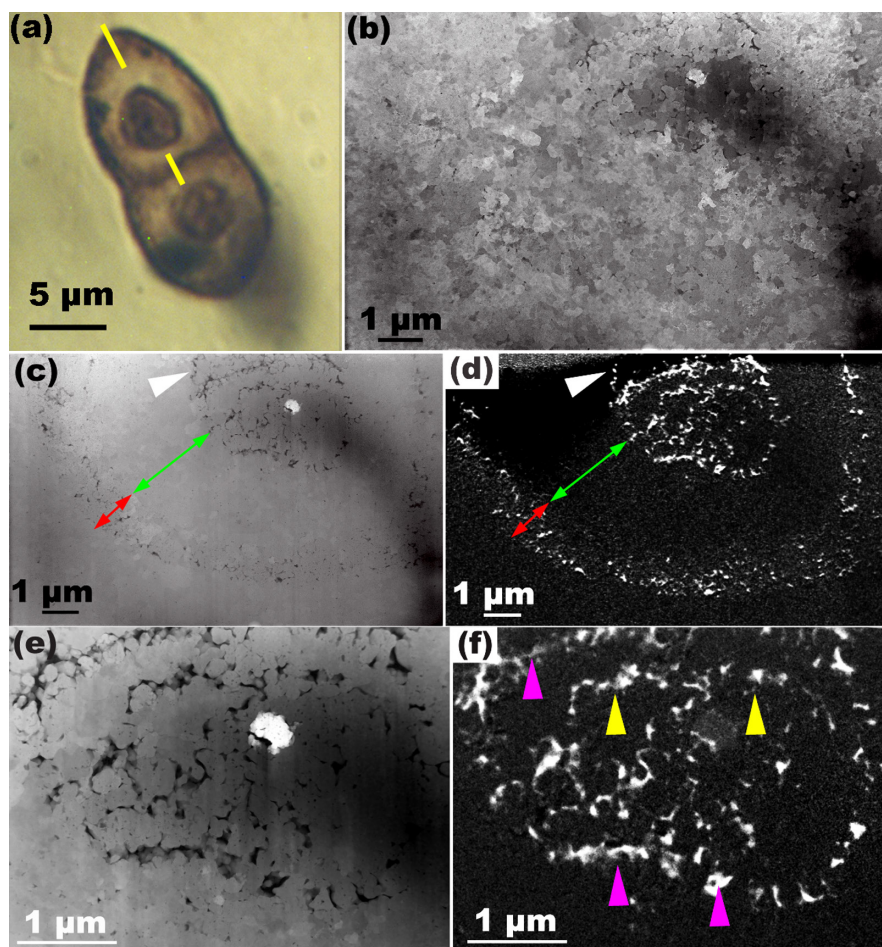


**FIGURE 5** | *Gloeodiniopsis mikros* (specimen 1). (a) Single-plane photomicrograph in transmitted light. Yellow dashes highlight the extremities of the FIB section part shown in b–d. In between is seen the cellular structure. (b) Dark-field STEM image of one cell from the FIB section showing the presence of quartz nano-crystals (various shades of gray) within and outside the microfossil. (c) HAADF STEM image of the area in b showing the distribution of the organic matter (in dark) and quartz (gray). The crystal in white is probably pyrite. (d) EFTEM map of carbon (in white) from the cell in (c). The red arrows in c–d highlight a  $\sim 0.5$ – $1\ \mu\text{m}$  large peripheral band of organic matter nanoparticles. The green arrows highlight an intermediate zone depleted in organic matter. The white arrowheads highlight an additional carbonaceous layer that extends from the coalescent spheroids forming the central vesicle. (e) HAADF image of the central vesicle. (f) EFTEM map of e showing the carbon distribution in the central vesicle. Yellow arrowheads highlight two ovoid individuals surrounded by a common, coalescent layer (pink arrowheads). Sample: P4353-11A.

layer that appears as the section of two coalescent hemispheres (pink arrowheads, Figure 5f) encompasses two additional layered structures (yellow arrowheads); another layer appears to branch from the outer layer of the vesicle (white arrowheads in Figure 5c,d). In specimen 1b, the grazing orientation of the FIB section with respect to the central vesicle only reveals a reticulated texture. In specimen 2, at least two concentric layers are discerned (Figure S7a–c). The outer layer is contorted in shape, and the central layer appears highly folded. All these layers forming the internal vesicles are sub-continuous, with minimal observable thicknesses of ca. 10 nm, reaching up to 200 nm locally for the outer layer, and up to 100 nm locally for the innermost layers.

#### 4.6.3 | Interpretations

Particulate outer layers were observed in *Glenobotrydion* coccoids of the Bitter Springs Formation by Oehler (1976a), who interpreted these organic particles as the remains of mucilaginous envelopes (sheath) or extracellular polymeric substances

(EPS). We similarly interpret the particulate outer structure as the outer sheath of the *G. mikros*. Indeed, sheaths can be silicified early while the cells are still preserved (Oehler 1976b; Westall, Boni, and Guerzoni 1995; Phoenix, Adams, and Konhauser 2000; Gong et al. 2020). Since the quartz grain size is homogenous among all cellular ultrastructures, we cannot distinguish whether the sheaths have been silicified earlier or at the same time than the cellular contents.

The broad organic-poor zone between the outer sheath and the inner vesicles may represent a zone where sheath material was not preserved or a zone in which cellular material underwent contraction. Such a contraction of cellular material has been inferred for microfossils of the Bitter Springs Formation (Knoll and Barghoorn 1975; Golubić and Barghoorn 1977; Knoll and Golubić 1979). Indeed, shrinkage of cells within their polysaccharide sheath without deformation of the latter is a common feature of early decay of cyanobacteria, with (Konhauser et al. 2004) or without silicification (Knoll and Barghoorn 1975; Golubić and Hofmann 1976).

Despite this probable contraction of the cell, cellular ultrastructure appears to be preserved in the central vesicles of these microfossils. The ultrastructure of the internal layers is subcontinuous and thus distinct from the nanoparticulate sheaths. These intracellular structures are layered, and may thus be interpreted in different fashion based on the modes of cell decomposition observed in cyanobacteria. The thicker layer forms the outer margin of the vesicles, and may accordingly represent all or a part of the cell envelope, such as the peptidoglycan. The peptidoglycan of cyanobacteria is usually less than 40 nm in thickness (Hoiczky and Hansel 2000). Although the outer layer of the vesicles is locally thicker than this (up to ca. 200 nm), local increases in thickness may tentatively be explained by the contraction of the envelope and subsequent imprint of the quartz grains, ca. 100 nm large, that may have displaced OM locally during (re)crystallization.

The innermost layers may represent cytoplasmic membranes or thylakoids—the photosynthetic membranes. These innermost layers appear generally thicker than cytoplasmic and thylakoids membranes (< 10 nm; Hoiczky and Hansel 2000; Liberton et al. 2006; van de Meene et al. 2006). Taphonomic increase in membrane thicknesses may result of shrinkage, but also possibly of fusion with various adjacent organic materials derived from phycobilisomes, cytoplasm, glycogen granules, ribosomes, and/or lipid bodies present in the cells. Cellular membranes can survive the degradation of the peptidoglycan in some taphonomic routes (Zheng et al. 2013). Possible plasma membranes, still attached to thicker wall ultrastructure have been documented in the Bitter Springs microfossils (Oehler 1976a). Photosynthetic membranes are highly resistant to fast bacterial lysis (Daft and Stewart 1973), and they can be preserved after cell envelopes have degraded (Zheng et al. 2013). Thylakoid membranes have been reported in ca. 600-year-old sediments (Lepot et al. 2014), in Cretaceous rocks (Pacton, Gorin, and Fiet 2008), and more recently in ca. 1 Ga and 1.73–1.78 microfossils (Demoulin, Lara, et al. 2024). Some layered organic material preserved in phosphatic intracellular inclusions in 1 Ga rocks (figure 5C in Wacey et al. 2019b) may similarly derive from photosynthetic membranes. However, in these unassigned microfossils other organelles and collapsed ultrastructures of eukaryotic origin may also be considered (Wacey et al. 2019b).

Here, the total number of concentric layers clearly evidenced in the vesicles is two, which is not sufficient to distinguish a few cell envelope components (peptidoglycan, membrane) from thylakoids (most commonly occurring in higher numbers, Mareš et al. 2019). The coalescent structure surrounding layered structures apparently forming two individuals in specimen 1a (Figure 5f) could correspond to an invaginating septum that was forming around two newly divided cell membranes. The additional layer pointed by white arrowheads in Figure 5d may be explained by infolding of the envelope (Oehler 1976a). This model where all the internal layers in *G. mikros* derive from the cell envelope requires the detachment of these layers, which appears plausible in some taphonomic routes (figure 8 in Berliner et al. 1987). Alternatively, the innermost layer, or all of the inner vesicle layers may derive from thylakoids. We note that concentrically layered internal vesicles have been observed in ca. 3.4 Ga spheroidal dubiofossils, which have been interpreted as abiotic biomorphs formed

by deposition of carbonaceous matter onto spherulitic silica or the result of diffusion of carbonaceous matter (Coutant et al. 2022). Here, the contorted and folded shapes of the layers within *G. mikros* and the sub-continuous texture of their organic matter are not consistent with such an abiotic morphogenesis scenario.

## 4.7 | *Sphaerophycus* Coccoids

### 4.7.1 | Assignment

We analyzed a second dyad of coccoidal microfossils displaying inner spheroidal vesicles (~5 μm in diameter) surrounded by a single common envelope. We assigned this microfossil to *Sphaerophycus medium* (?) rather than *Gloeodiniopsis mikros* due to the higher relative volume of the inner vesicle compared to the envelope, the granular texture of the inner vesicles (Figures 6a versus 5a) and the presence of similar specimens containing more than four inner vesicles in the vicinity of the analyzed microfossils. The morphological similarity with the extant genus *Aphanocapsa* and the binary division/fission patterns of other *Sphaerophycus* microfossils argue for a cyanobacterial origin (Knoll 1982; Knoll, Sweet, and Mark 1991).

### 4.7.2 | (S)TEM Imaging

FIB sectioning intercepted the two inner vesicles and their enclosing envelope (Figure 6a–c). Again, the microfossil is associated with quartz nanocrystals (~200–400 nm in diameter). The dyad is enclosed in an outermost envelope formed by a discontinuous cloud (~1-μm thick) of organic particles smaller than 100 nm (Figure 6c,e). Each vesicle of the dyad is outlined by another similar, but internal, discontinuous envelope composed of small organic particles (Figure 6c,e). A third, innermost layer occurs within the right cell of the microfossil (white arrows in Figure 6). The left cell, in contrast, does not show this innermost envelope but has a small internal patch of organic nano-granules (Figure 6f).

### 4.7.3 | Interpretations

We interpret the outer particulate layer as the remains of an extracellular sheath, as discussed above for similar structures in *G. mikros*. Based on their particulate aspect, the layers delimiting the inner vesicles also likely represent sheath-derived structures. Indeed, coccoid (as well as filamentous cyanobacteria) may present multi-lamellar sheaths (Gonzalez-Esquer et al. 2016) that appeared resistant to drastic basic and acid chemical treatments (Chalansonnet et al. 1988). This multiple layering further distinguishes this microfossil from the studied *Gloeodiniopsis* (Figure 5).

The innermost layer seen in part of the rightmost cell is thinner and less granular than the inferred sheath layers, hence it may represent a remnant of the cell envelope (peptidoglycan ± membrane) of the microorganism (Oehler 1976a). In contrast, the inner patch in the left cell might represent the remains of internal organic material of the cell and/or shrunk and fused organic



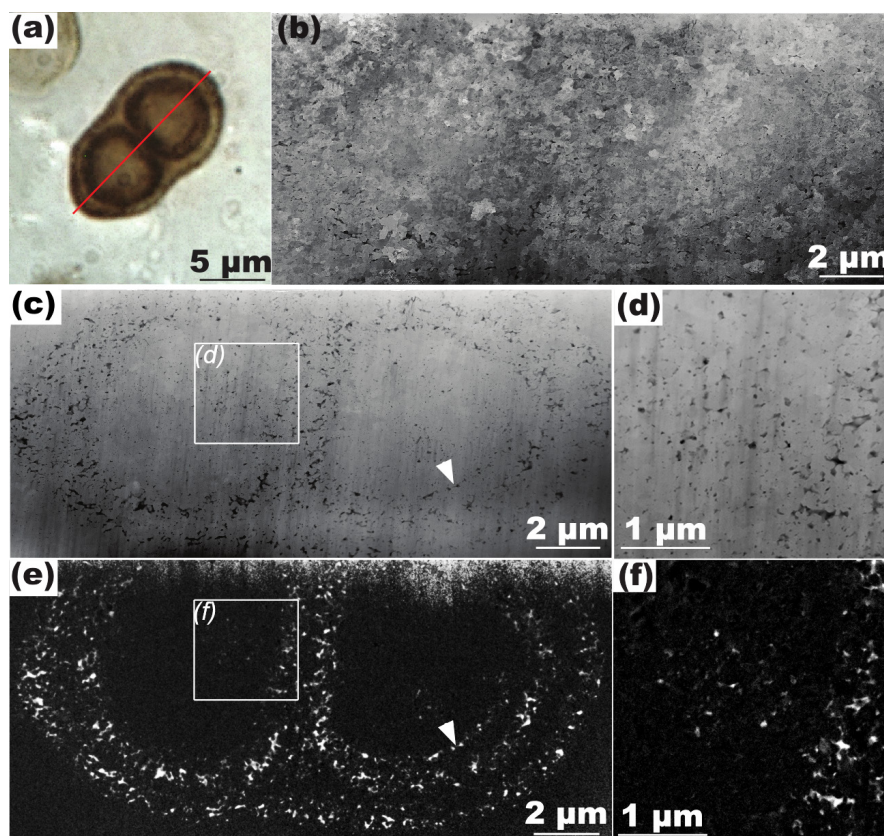


**FIGURE 6** | *Sphaerophycus* dyad. (a) Photomicrograph in transmitted light (Red line: FIB section position). (b) Dark-field STEM image of the FIB section showing the presence of quartz nano-crystals (in various shades of gray) within and outside the microfossil. (c) HAADF STEM image of the area in b showing the distribution of the organic matter (in black) and quartz (gray). (d) Zoom on the zone boxed in c. (e) EFTEM elemental map showing the carbon distribution of the FIB section. (f) Zoom of the zone boxed in e showing the position of an internal organic patch in the left part of the dyad. In c and e, the white arrowheads indicate the position of an innermost layer. Sample: P4353-11A.

membranes (Oehler 1976a). Investigation of some early stages of cell degradation (Daft and Stewart 1973; Zheng et al. 2013) and of buried sediments (Pacton, Gorin, and Fiet 2008; Lepot et al. 2014) have shown that some intracellular contents such as the photosynthetic membranes of cyanobacteria can be preserved without preservation of surrounding cell wall and/or cytoplasmic membranes.

The distinct ultrastructures observed in two different cells of the *Sphaerophycus* microfossil show the difficulty of constraining the nature of the layers of organic matter present in coccoidal Precambrian microfossils due to the possible fusion of various organic materials (sheaths/capsules, membrane, cellular material) during lysis and silicification.

## 4.8 | *Synodophycus* Coccoids

### 4.8.1 | Assignment

*Synodophycus* microfossils were first reported by Knoll (1982). The type species *Synodophycus euthemos* consists of large pluricellular colonies composed of 16 to 64 small vesicles (4–7 μm in cross-sectional diameter). The wall structure of individual vesicles is thin while the envelope of the colony studied here appears thicker (Figure 7a). *Synodophycus euthemos* has been interpreted as the fossil of pleurocapsalean cyanobacteria

(family *Xenococccaceae*, Waterbury and Stanier 1978) based on the (uncommon) presence in some vesicles of inner 1–2 μm vesicles interpreted as baeocytes formed by multiple fission in enlarged cells (Knoll, Sweet, and Mark 1991). Although the fossil studied here lacks baeocytes, the relatively large size of the cells, their small number in the colony and the outer envelope links them to *Synodophycus euthemos* and contrast with the other colonial microfossil population of the Draken Formation, *Coniunctiophycus* (incertae cedis, Knoll, Sweet, and Mark 1991), which aggregates more but smaller cells.

### 4.8.2 | (S)TEM Imaging

One FIB section was extracted from the *Synodophycus* colony in Figure 7a. The quartz crystals within and outside of the colony are ~200–500 nm in diameter (Figure 7b). The outer layer of the colony is composed of a <1 μm thick discontinuous layer, which contains small organic matter grains (<100 nm in diameter). Each vesicle within the envelope is also delimited by a thinner (<400 nm, mostly <150 nm) layer of organic nanograins (Figure 7d,e). These internal layers observed in *Synodophycus* are relatively poor in organic matter and may represent a different type of ultrastructure. The limit between the internal and outer layers is not clearly observable (Figure 7e). In addition, triple junctions formed by the intersection of two internal layers and the external layer are

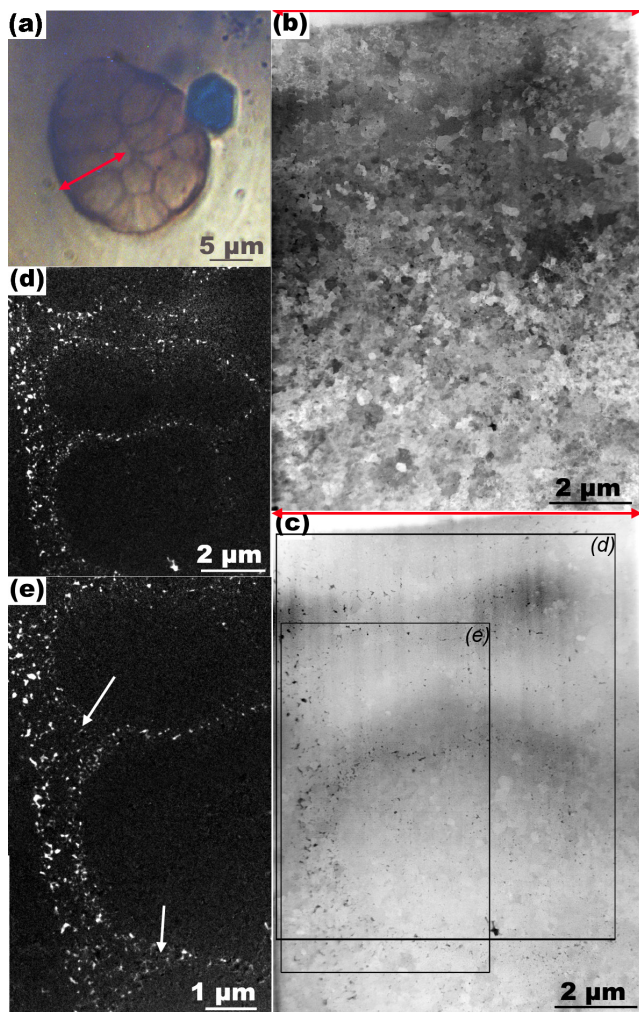


**FIGURE 7** | *Synodophycus euthemos*. (a) Photomicrograph in transmitted light (red line: FIB section position). (b) Dark-field STEM image of the FIB section (red line indicates the part at the surface of the petrographic section and same position as in a). Quartz nano-crystals (in various shades of gray) form the matrix within and outside the microfossil. (c) HAADF STEM image of the FIB section (same red line position as previously) showing the distribution of organic matter (in dark) and quartz (gray). (d, e) EFTEM map showing the distribution of carbon (in white) from several cells boxed in c. The white arrows in e indicate the accumulation of kerogen at the junction of the outer envelope and internal cell walls. Sample: P4353-11A.

commonly populated by organic matter, thus forming a local thickening (white arrows in Figure 7c–e).

#### 4.8.3 | Interpretations

This discontinuous granular texture of the outer organic layers is reminiscent of that of the sheaths surrounding the coccoid microfossils discussed above. Based on these different features of the internal layers, we interpret all the internal organic layers as the remnants of F-layers that are the fibrillar outer wall layers of pleurocapsalean cyanobacteria (Waterbury and Stanier 1978). Nevertheless, we note that fused cell walls have also been observed in non-pleurocapsalean fossils of the Bitter Springs Formation (Oehler 1976a). The fibrillar

structure observed in the outer walls of pleurocapsalean cyanobacteria is also found in some sheaths of filamentous cyanobacteria, as noted by Waterbury and Stanier (1978) as well as some section V cyanobacteria such as *Chlorogloeopsis fritschii* (Baulina 2012). Thus, although the F-layers are closely attached to the outer membranes of pleurocapsales (Waterbury and Stanier 1978), they may share similar fossilization patterns as sheaths.

## 4.9 | *Polybessurus* Stalked Coccoids

### 4.9.1 | Assignment

*Polybessurus* microfossils are composed of thick-walled multi-laminated organic stalks with cup-shaped morphology formed by unidirectional—usually vertical—secretion of polysaccharides (Green et al. 1987). *Polybessurus* have been interpreted as cyanobacteria based on their unequivocal similarity with extant *Cyanostylon* (Chroococcaceae, which forms crusts on tidal flats of the Bahamas: Green et al. 1987; Knoll, Sweet, and Mark 1991; Knoll 2003). These microorganisms occur as unicells that “jet” upward from the sediment surface by the highly unidirectional secretion of extracellular polysaccharide stalks (Green et al. 1987).

### 4.9.2 | STEM Imaging

Two FIB sections were extracted from *Polybessurus* microfossils (Figure 8a, Figures S8, S9). Both displayed one to two dark internal envelopes surrounded by a jetted stalk with multiple thin laminae. These two *Polybessurus* specimens are permineralized in nano-quartz (200–400 nm in diameter; Figures S8a,b, S9a,b). The FIB section of *Polybessurus* specimen 2 only intercepted the layered stalk, which displayed one or two thick layer(s) composed of organic nanograins (Figure S9). The FIB section of *Polybessurus* specimen 1 (Figure 8) intercepted both stalk with thin nanogranular layers and a darker central structure. Specimen 1 comprises more than seven concentric spherical envelopes, which appear thin compared to the sheaths of *Gloeodiniopsis* and *Sphaerophycus*. The two/three innermost layers are well defined, while the outermost layers appear less continuous and thinner. Moreover, the inner envelopes display more abundant organic matter nanograins than the outer, thinner envelopes (Figure 8b–d). These three inner layers display triple junction (red arrow in Figure 8c), and invagination of the most central (outlined by the red line in Figure 8c).

### 4.9.3 | Interpretation

The nanogranular carbon distribution in the layered stalks are coherent with those of sheath structures observed in the other Chroococcacean microfossils *Gloeodiniopsis* and *Sphaerophycus* (Figures 5, 6). The outer, thinner layers of organic matter (yellow bracket in Figure 8c) certainly belong to the laminated stalk-forming polysaccharide structure. The 2–3 discontinuous central layers of specimen 1 (Figure 8) may result from one to two infolded envelopes. Such structure



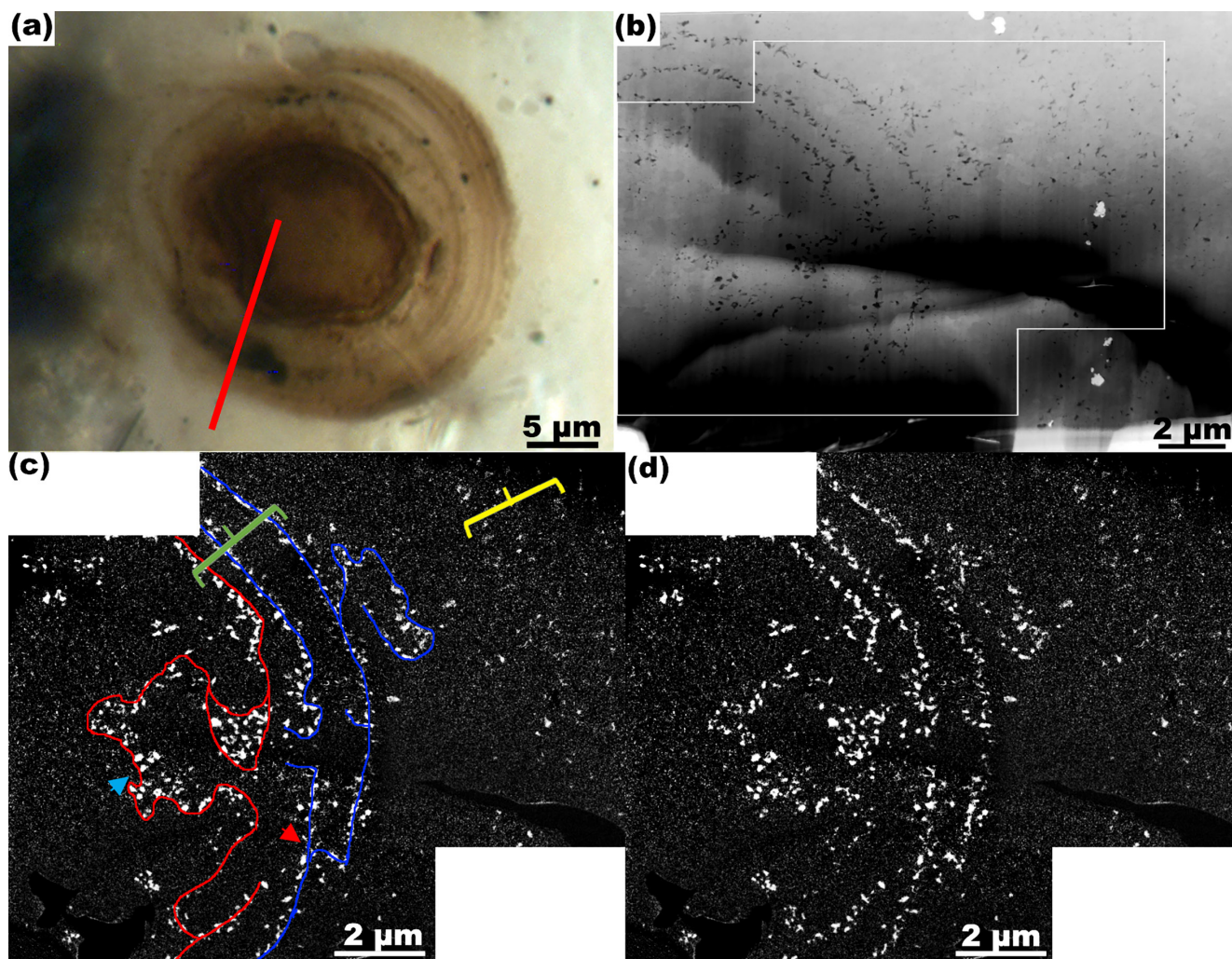


**FIGURE 8** | *Polybessurus* specimen 1. (a) Photomicrograph of the microfossil in transmitted light (red line: Position of the FIB section through the sheath structure of the stalk and the cell). (b) HAADF STEM image of the FIB section. Carbon appears in dark and quartz in gray. Pyrite appears in bright white. Note that the large dark zone correspond to holes caused by FIB damage. (c) EFTEM map of carbon (in white) in the area boxed in b. Green bracket: Set of thicker internal layers outlined by red and blue lines. Red arrow: Triple junction suggesting infolding of the internal layer set. Blue arrow: Internal layered organic material formed by the invagination of the innermost envelop outlined in red. Yellow bracket: Set of thinner external layers in the stalk. (d) Same as c without annotations. Sample: P4353-6A.

suggests that the internal layers could represent the envelope of the cell during an early stage of its life cycle (Green et al. 1987). The invaginated and/or folded structure of the innermost layers of specimen 1, as well as their increased thickness suggests that these could represent layers of the cell envelop, possibly including membranous contents as discussed above for *Gloeodiniopsis* microfossils. Unfortunately, no ultrastructural data are available for modern *Cyanostylon*, hindering the interpretation of these internal layers. Alternatively, they could represent sheaths and/or the innermost stalk-forming polysaccharide layers.

#### 4.10 | *Myxococcoides* spp.

##### 4.10.1 | Assignment

The different microfossil assemblages present in the cherty lenses contain remains of various allochthonous microorganisms, dominated by spheroidal microorganisms of the

genus *Myxococcoides* (Knoll, Sweet, and Mark 1991). These spheroidal microfossils (10–20  $\mu\text{m}$  in diameter) are randomly dispersed in the different microbial assemblages and occur isolated or in colonies (Figure 9a, Figure S2e). These microfossils are generally preserved as dense, thick walls, although they can contain internal material, including pyrite crystals (e.g., Figure 9). *Myxococcoides* may comprise algae and/or (cyano)bacteria; even domain-level phylogenetic interpretation is difficult due to their simple shape (Knoll, Sweet, and Mark 1991).

##### 4.10.2 | (S)TEM Imaging

Two FIB sections were extracted from these microfossils (Figure 9; Figures S10, S11). The quartz crystals inside and outside the microfossils are ~100–400 nm wide (Figure 9d,e, Figure S11b). The cross-sectional structure of the wall of these microfossils forms a well-defined layer of ~0.5 to ~0.9  $\mu\text{m}$  in thickness (specimens of Figure 9, Figure S11, respectively).



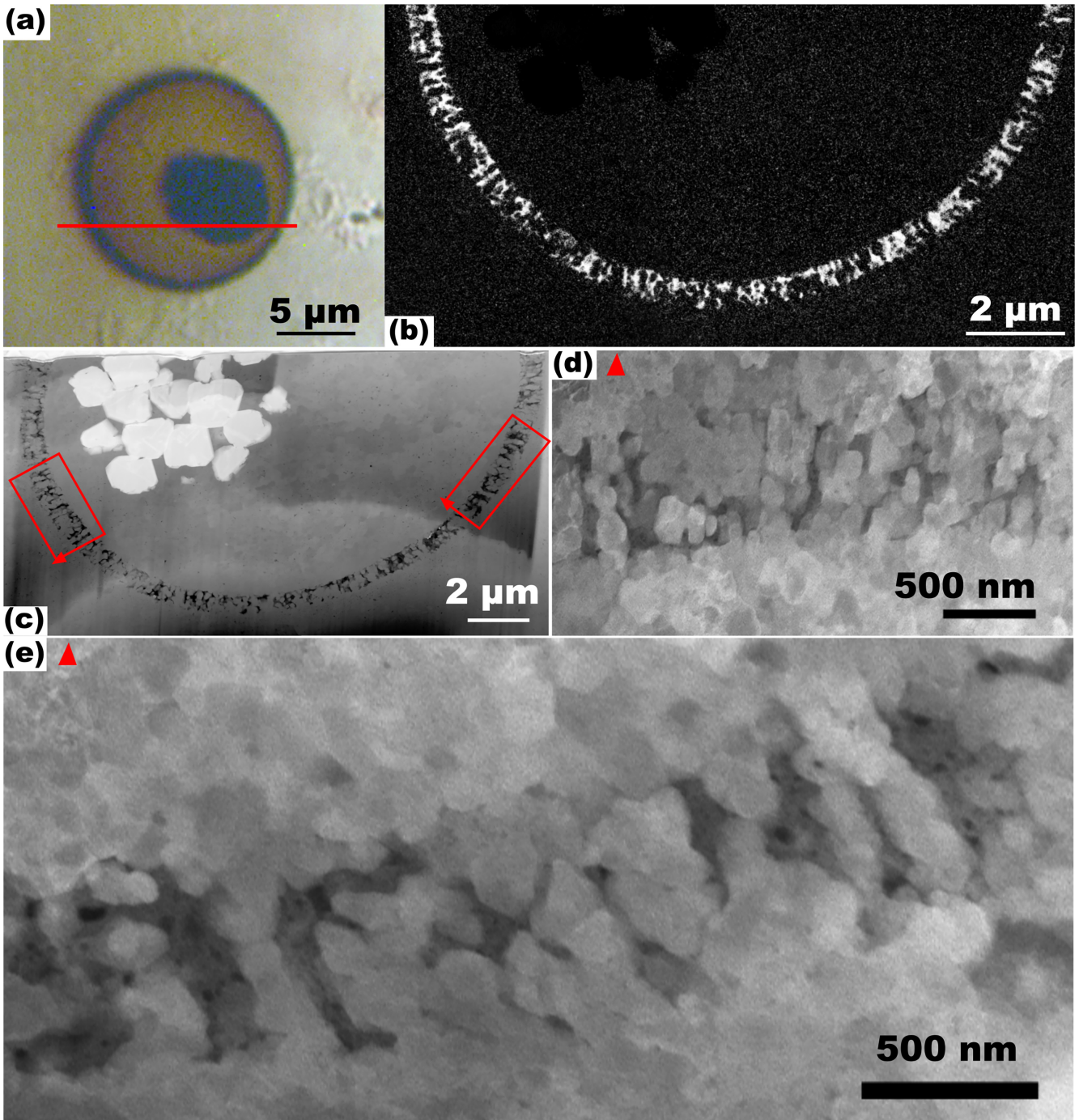


**FIGURE 9** | *Myxococcoides*. (a) Photomicrograph in transmitted light (red line: FIB section position). (b) EFTEM elemental map of carbon showing the distribution of organic matter of the FIB section cut along the line in a. (c) HAADF-STEM image of b showing the distribution of organic matter (dark), quartz (gray), and iron sulfide (white, EDX spectrum: Figure S10d). (d, e) Dark-field STEM images of the boxed zones at the left and right in c, respectively (red arrows indicate directions) showing the pillared alignments of organic matter (dark gray) and quartz (various, lighter shades of gray) in the cell wall, and nanoporosity (black) in organic matter. Sample P4353-11A.

The outline of these layers is continuous, but characterized by a series of columns of organic matter and nano-quartz oriented in a sub-radial fashion (Figure 9, Figure S11d–e). These columns form “bridges” between the inner and the outer limits of the wall. This organic matter is nanoporous (Figure 9e). One *Myxococcoides* individual shows an outer diffuse layer of small organic grains (<200 nm) surrounding the pillared layer (Figure S11e).

#### 4.10.3 | Interpretations

The ultrastructure of *Myxococcoides* observed here is different from that of the spheroidal microfossil observed by TEM by Foucher and Westall (2013). The previously analyzed *Myxococcoides* was composed of a thin continuous wall structure (<200 nm thick) and internal organic material which have been interpreted as the membrane and the cytoplasm of

the microorganism, respectively (Foucher and Westall 2013). This relatively thin wall could correspond to a (cyano)bacterial envelope rather than a eukaryotic cell wall, consistent with conclusions of Oehler (1976a). *Myxococcoides minor* of the Bitter Springs Formation displays similarly thin walls (Schopf 1970; Oehler 1976a) and was accordingly interpreted as cyanobacterial. Interestingly, C-isotopic microanalyses have distinguished the isotopic composition of *Myxococcoides* sp. ( $\delta^{13}\text{C}_{\text{org}} = -22.6 \pm 0.5\%$ ) from those of spatially associated *Leiosphaerida crassa* ( $\delta^{13}\text{C}_{\text{org}} = -28.9 \pm 1\%$ ) in ~775 Ma cherts of the Chichkan Formation (Williford et al. 2013), consistent with the hypothesis that the former were cyanobacteria while the latter were eukaryotes. The outer layer of the *Myxococcoides* observed here is much thicker (up to ~0.9  $\mu\text{m}$ , Figure 9 and Figure S11) than in the aforementioned occurrences.

The organic matter within the wall structure fills the spaces between quartz crystals that align to form radially-elongated fibers. This pillared structure might have resulted of infilling of a primary porous ultrastructure of the microorganism during the primary silicification event, as further discussed below. Alternatively, this structure might have resulted from a rapid early encrustation of the cell interior and exterior by amorphous silica (i.e., opal A). Then, the space between the different cell membrane(s)/wall(s) may have been impregnated with a second, more porous generation of silica, giving the outer wall this structure after nanoscale migration of the organic material in pores between silica grains. Three taphonomic scenarios can be proposed. (i) The development of this columnar fabric might be due to the capacity of the organic matter to slow the crystallization of quartz (Alleon et al. 2016a). Such taphonomic process might be related to that forming the indentation patterns reported by Wacey et al. (2012) and Lekele Baghekema et al. (2017) in fossil sheaths and cell walls. (ii) Similarly, silica may have formed a crust of nanograins (30–200 nm) on the external surface of an organic layer, as observed on sheath structures of cyanobacteria (Phoenix, Adams, and Konhauser 2000; Konhauser et al. 2004; Benning et al. 2005). After the death of the microorganisms, the cell interior and exterior rapidly encrusted by opal A (Herdianita et al. 2000; Lynne et al. 2005; Preston et al. 2008). Later during diagenesis, the organic matter from outer structures such as sheath/capsule and/or wall may have migrated and filled the spaces between the grains of the crust. (iii) Alternatively, quartz pillar may have grown through decaying wall. In these three taphonomic scenarios, it would be expected that quartz would grow inside any porous zone within the wall, locally forming inner and outer carbonaceous layers. This is not observed here, as most of the bases of quartz pillars do not present organic remains. Such quartz growth would also push against the inner and outer wall boundaries, thus disrupting its apparent thickness. These two growth patterns would likely result in the thickness discontinuities and internal porosities as those observed by TEM in demineralized microfossils of the Bitter Springs Formation (Oehler 1976a). Here, in contrast, a very sharp boundary exists between randomly growing quartz inside/outside the wall, and a zone of pillared quartz and carbonaceous matter that altogether define a wall of homogenous thickness. It rather supports the alternative hypothesis that an original ultrastructural porosity

directed the growth of quartz through the wall before post-mortem alteration could disrupt the carbonaceous texture.

The pillared quartz structure might be inherited from precipitation of silica in a porous and/or radial ultrastructure such as the outer fibrillary wall layer of algae (Domozych, Wells, and Shaw 1992; Domozych 2011), or radial canals such as those observed in the walls of *Tasmanites* and their modern prasinophyte counterparts (Aroui, Greenwood, and Walter 2000; Moczyłowska 2011; Willman and Cohen 2011). The outer wall of Eocene dinoflagellates, ca ~1  $\mu\text{m}$  thick, also display pillared structures in the cross section (Moczyłowska and Willman 2009). Radially-developing fibers/pillars have also been observed in the envelope of cyanobacterial akinetes (Lang 1968; Miller and Lang 1968; Clark and Jensen 1969) and in the sheaths of filamentous cyanobacteria (Lang 1968). *Oscillatoria princeps*, a large (> 24  $\mu\text{m}$ ) filamentous cyanobacterium, forms exceptionally thick walls (up to 700 nm) with large pores (Hoiczky and Baumeister 1995; Mühlsteinová et al. 2018), but unicellular cyanobacteria have much thinner walls (Hoiczky and Hansel 2000). The amorphous organic matrix between fibers in filamentous cyanobacterial sheaths decays preferentially compared to the fibers (Daft and Stewart 1973), possibly generating radially-oriented pore space favoring silicification in pillars. A very thin layer (~200 nm) of fibrils was also observed around unicellular cyanobacteria (Stanier (Cohen-Bazire) 1988). Bacteria may also form fibrillary extracellular polysaccharides (Costerton, Irvin, and Cheng 1981). However, the sheaths and capsules of the six cyanobacterial morphospecies studied here did not form a dense organic layer such as that observed in the studied *Myxococcoides* and were rather preserved as diffuse clouds of nanoparticulate organic matter. Altogether, assuming that the pillared organic structure of the studied *Myxococcoides* is inherited from an original ultrastructure, its thickness (up to ~0.9  $\mu\text{m}$ ) and presence in spherical single cells (i.e., unlike akinetes) correlate best with fibrillary cell walls of eukaryotes. However, the dense internal layers of the cell wall such as the medium and inner layers (respectively 22 and 300 nm thick) reported by Domozych, Wells, and Shaw (1992) are absent, but this may be a result of taphonomic processes. Additional 3D analysis with confocal laser-scanning microscopy (Schopf and Kudryavtsev 2009), FIB-SEM tomography (e.g., Wacey et al. 2013) or sequential FIB milling (Schiffbauer and Xiao 2009) may help assess further the origin of this pillared ultrastructure.

The additional nanogranular outer layer observed in one specimen (Figure S11) might constitute residues of sheath and/or secreted mucilage. This interpretation is consistent with the preservation of sheaths in the mat-dwelling cyanobacteria (Figures 5, 6, and 8). Alternatively, the presence of these organic nanoparticles might reflect post-mortem outward displacement of organic matter from the wall structure (Knoll, Strother, and Rossi 1988). But in such case, similar small organic matter particles would also have migrated toward the inside of the cell, which is not the case. Thus, the interpretation of these organic particles as being remains of mucilage or an additional sheath appears more likely.

A rather low quantity of organic matter can be observed within one *Myxococcoides* cell (Figure S11e). As observed



by Oehler (1976a) and in some microfossils described above (Figures 5, 6), such organic matter patches may be the residues of internal material and membranes that have shrunk and fused after the lysis of the micro-organisms and during silicification. The presence of Fe-rich minerals such as pyrite (Figure 9) and iron-carbonates zoned in barium (Figure S11) coated and/or closely associated with organic nanograins (Figure S11e) suggests that other *post-mortem* processes, possibly bio-mediated, occurred in addition to lysis and silicification. The simultaneous presence of organic matter and iron sulfide suggests some heterotrophic sulfate-reducing bacterial activity, while the iron carbonate may have formed either via microbial or thermal iron reduction (Hendry et al. 2000; Bernard et al. 2007; Koehler et al. 2013; Posth et al. 2013).

## 4.11 | Large Spheroid With Ruptured Wall

### 4.11.1 | Assignment

Rarely, larger (~80–120  $\mu\text{m}$  in diameter) spheroids occur in Draken cherts. We focused on an individual with a ruptured wall on one side of the cell (Figure 1a, Figure S2a–g). In some ways, this fossil resembles VSMS found widely in upper Tonian sedimentary rocks (Porter and Knoll 2000; Porter, Meisterfeld, and Knoll 2003; Bosak et al. 2011; Cohen, Irvine, and Strauss 2017; Riedman, Porter, and Calver 2018; Morais et al. 2019; Martí Mus, Moczyłowska, and Knoll 2020), including Spitsbergen (Martí Mus, Moczyłowska, and Knoll 2020). The fossil in question, however, lacks diagnostic features of VSMS, including a thick (ca. 2  $\mu\text{m}$ ) wall and a distinctly differentiated collar surrounding the apical opening. Moreover, in most places, including

Spitsbergen, VSMS are preserved as originally pyritized (and commonly oxidized during diagenesis) walls and/or silica infilling of cell interiors. The cell under consideration is more parsimoniously interpreted as a ruptured spheroidal cell, perhaps a cyst that originally contained cells like the *Myxococcoides* fossils found in association with it (see, for example, Knoll, Sweet, and Mark 1991, figure 11.3). The microfossils appear granular under the optical microscope (Figure 10a, Figure S2g).

### 4.11.2 | (S)TEM Imaging

TEM characterization of an FIB section extracted from a specimen revealed two distinct layers. The internal layer is composed of small organic matter grains (<300 nm in diameter) (Figure 10b,c). This layer is impregnated with nanoquartz (200–400 nm in diameter), similar to the internal and external parts of the microfossil. It displays rare iron minerals, probably oxides according to EDX data (map in Figure S12c). A thicker outer layer of organic matter is irregular and appears to pinch and swell irregularly between micrometric quartz crystals (Figure 10b,c). This outer layer displays nanopores with a heterogeneous distribution and highly variable dimensions (sometimes >100 nm large, Figure S12d) that appear similar to those in a *S. svalbardensis* microfossil (Figure 4d) and contrast with the smaller (<20 nm) and homogeneously spread pores in the central thread of *Siphonophycus* (Figure 3d). Micrometric quartz crystals also locally extend outside the microfossil (black arrows in Figure 10b). The granular envelope is composed of large, dense organic grains (or sheets), which seem to fill the spaces between coarse quartz grains (Figure 10).

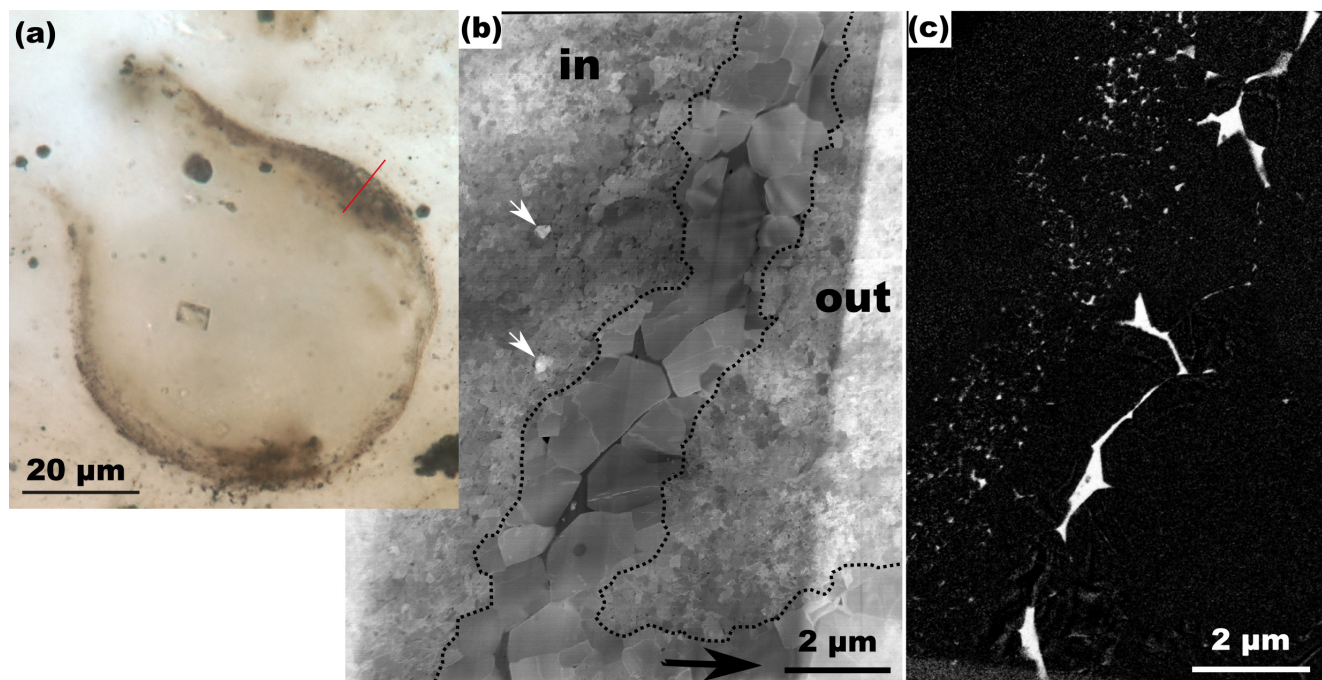


**FIGURE 10** | Large spheroids with ruptured wall. (a) Single plane photomicrograph in transmitted light 2  $\mu\text{m}$  below the surface (Red line: FIB section position). (b) Dark-field STEM image of the FIB section showing the presence of coarse quartz crystals (zone outlined with dashed lines) associated with the wall structure of the microfossil. A zone of coarse quartz extends outside of the microfossil wall into the nano-quartz matrix (black arrow). White arrows show Fe-minerals (see Figure S12). (c) EFTEM elemental carbon map of the FIB section showing the distribution of the organic matter. Sample: P4353-1B.

### 4.11.3 | Interpretations

The association of dense organic matter with coarse quartz in this microfossil is reminiscent of what was observed in filament specimen 1 (Figure 3b). Such similarity between these different microfossils suggests that both have been affected by similar diagenetic process, despite an initial different nature. As discussed for filament specimen 2, it is unlikely that this innermost layer of nanoparticles embedded in nanoquartz formed through migration from the outer, thicker organic envelope, as nanoparticles would be also expected in the nanoquartz lying outside the microfossil. This suggests that two distinct envelope ultrastructures have been preserved in the large spheroidal fossil. The heterogeneously sized and distributed porosity observed in the outer wall is consistent with that observed in microfossils as well as solid bitumen (Versteegh et al. 2004; Bernard and Horsfield 2014; Katz and Arango 2018). We note, however, the similar Raman spectra observed between the inner, nanoparticulate wall and the thicker/clotted outer wall, observed in this specimen (Figure S2g) and other microfossils (Figure S2b,d) within this chert clast (Figure S3, Table S1: fossil wall versus fossil clot). The Raman spectra of these fossils are distinct from those of the bitumen vein analyzed in another sample, consistent with the hypothesis that at least part of the microfossil organic matter comprises indigenous kerogen.

## 5 | Summary

Raman and XANES spectroscopy indicate that the insoluble organic matter in Draken microfossils is highly mature, mostly aromatic, but not highly graphitic. One sample revealed bitumen migration in small veins, but the distinct Raman spectroscopic signatures of microfossils argue that they largely comprise indigenous kerogen, even if a contribution of ambient or exogenous pyrobitumen cannot be ruled out. In spite of the high maturity, a degree of morphological detail comparable to that observed in less mature Bitter Springs microfossils can be observed in FIB sections. All the microfossils present here are embedded and filled by nanoquartz, contrasting with the larger quartz crystals observed in other rocks with a better organic Raman index of preservation (Schopf et al. 2005). Indeed, some acritarchs from the ca. 650 million years old Chichkan Formation display micrometric internal crystals (Kempe et al. 2005) not seen here, and larger submicrometric to micrometric quartz crystals occur in some microfossils of the Gunflint Formation (Lepot et al. 2017, but see Wacey et al. 2012). In the Draken Formation, the small size of the quartz crystals allowed for preservation of a variety of ultrastructures. These cannot be resolved completely using optical microscopy, but they become clear at the TEM scale. These preserve a petrographic link between organic matter and quartz, allowing us to address taphonomic processes.

We have described the ultrastructure of microfossils that have been interpreted previously as chroococcalean cyanobacteria (*Gloeodiniopsis mikros*, *Sphaerophycus*), pleurocapsalean cyanobacteria (*Synodophycus euthemos*), sheathed filamentous cyanobacteria (*Siphonophycus*, *S. svalbardensis*), and *incertae sedis* (*Myxococcoides*) as well as large spheroids.

Our observations show that the sheath structures of some *Siphonophycus* and of all the *Chroococcales* cyanobacteria microfossils studied here are preserved as bands of nanogranular organic matter. Some *Siphonophycus* display thin, single-layered outer layer, which can be interpreted either as the preservation of a thin sheath or of a tubular, longitudinal outer envelope, which may be devoid of cross-walls. Double nanogranular sheath layers are observed in *Sphaerophycus* coccoids. In *Synodophycus euthemos*, fusion of walls and formation of organic-rich triple junctions at the intersection with the external layer is consistent with the preservation of fibrillar outer wall layers typical of pleurocapsalean cyanobacteria. The ultrastructure of *Polybessurus* stalks shows similar organic distribution as those observed in sheaths of the other coccoid microfossils. Moreover, our observations show that the inner microfossil structure is composed of thicker wall/sheath layers, which may represent the earliest stages of the stalk formation.

The origin of possible cellular envelopes and intracellular content was investigated in both coccoid and filamentous microfossils. Based on comparisons with taphonomy of modern cyanobacteria, we constrain the nature of the internal layers in *Gloeodiniopsis mikros*. Their contraction in the sheath and their sub-continuous structure distinct from the nanoparticulate sheath argue that they represent detached envelop layers (peptidoglycan and/or cellular membranes), and/or photosynthetic membranes (thylakoids). In any case, their apparently enhanced thickness compared to such primary ultrastructures requires shrinkage and/or the condensation of labile internal cellular materials onto resistant layered ultrastructures. Some innermost layers in *Sphaerophycus* and *Polybessurus* coccoids may similarly represent preserved envelopes or membranous ultrastructures.

In contrast, nanoscale analyses of a trichome from *S. svalbardensis* indicate that only the general shape of the cells is preserved (as a ghost structure with the nanoquartz matrix), but not the cell wall. Granular to thread-like internal OM structure in *Siphonophycus* may correspond to diagenetically polymerized in situ cell material (with obliterated morphology), with possible addition of ambient lipids/bitumen molecules.

The *Myxococcoides* observed here reveal an outer layer composed of unusual radial pillars of organic matter. This structure—to our knowledge never observed by previous studies—and only observable at the nano-scale, appears best interpreted as derived from original cell wall ultrastructure. As such, it may represent eukaryotic cell wall and/or structures of cyanobacterial sheaths or cyanobacterial akinetes. A eukaryotic affinity is best reconciled with the wall thickness, size and lack of dividing cells of *Myxococcoides*.

Finally, we examined the ultrastructure of a large carbonaceous spheroid of uncertain phylogenetic affinities. These microfossils are composed of two distinct organic layers: an inner layer composed of organic nanoparticles and a thicker organic outer layer forming a reticulated envelope at the microscale. Experimental taphonomy coupled with ultrastructural analysis and spectro-microscopy (e.g., STXM-XANES) is required to further constrain the interpretation of this fossil.

The microfossils are all preserved in nano-quartz matrix, consistent with the long held hypothesis that rapid silicification enhances organic structure preservation. However, coarser quartz crystals are always associated with displacement (at least, locally) of organic matter. In addition, organic ultrastructures appear locally to highly discontinuous. These discontinuities could lead to fragmentation of microfossils during acid maceration, whereby specific ultrastructures could be removed or specific morphospecies destroyed, hence producing biases in structure and diversity of the fossils. Such observations on microfossils in over-mature rocks can help discuss the biogenicity, the nature of organic structure and the taphonomy on other unidentified or putative microfossils in Paleoproterozoic or Archean rocks. In particular, it may help distinguish metamorphosed microfossils from abiotic microstructures coated by discontinuous carbonaceous films (e.g., Coutant et al. 2022).

## Acknowledgments

David Troadec (IEMN) is highly thanked for the preparation of the FIB sections. Sylvie Regnier is thanked for help with the semi-thin section preparation. Philippe Recourt (LOG) is thanked for help with SEM. This work was carried out with the support of Diamond Light Source, instrument I08-SXL (proposal SP14784). We thank Tohru Araki, Burkhard Kaulich, and Majid Kazemian Abyaneh for help with STXM at the Diamond synchrotron facility. We thank Corentin Le Guillou (UMET) for help with STXM data. This work was also carried out with support of the the 10ID-1 beamline at the Canadian Light Source, which is supported by the NSERC, the CIHR, the NRC and the University of Saskatchewan. The Chevreul Institute is thanked for its help in the development of this work through the CHEMACT project supported by the "Ministère de l'Enseignement Supérieur et de la Recherche", the region "Hauts-de-France" and the "Métropole Européenne de Lille". The Chevreul Institute is thanked for its help in the development of this work through the ARCHI-CM project supported by the "Ministère de l'Enseignement Supérieur de la Recherche et de l'Innovation," the region "Hauts-de-France," the ERDF program of the European Union and the "Métropole Européenne de Lille." FIB work was partly supported by the French RENATECH network. This research was funded by the Agence Nationale de la Recherche (ANR-15-CE31-0003-01) and Région Hauts-de-France (project Vison-AIRR iM4) grants to K.L.

## Conflicts of Interest

The authors declare no conflicts of interest.

## Data Availability Statement

The data that support the findings of this study are available from the corresponding author upon reasonable request.

## References

- Agić, H., M. Moczyłowska, and L.-M. Yin. 2015. "Affinity, Life Cycle, and Intracellular Complexity of Organic-Walled Microfossils From the Mesoproterozoic of Shanxi, China." *Journal of Paleontology* 89: 28–50.
- Alleon, J., S. Bernard, C. Le Guillou, et al. 2016a. "Early Entombment Within Silica Minimizes the Molecular Degradation of Microorganisms During Advanced Diagenesis." *Chemical Geology* 437: 98–108.
- Alleon, J., S. Bernard, C. Le Guillou, et al. 2016b. "Molecular Preservation of 1.88 Ga Gunflint Organic Microfossils as a Function of Temperature and Mineralogy." *Nature Communications* 7: 11977.

- Arouri, K., P. F. Greenwood, and M. R. Walter. 1999. "A Possible Chlorophycean Affinity of Some Neoproterozoic Acritarchs." *Organic Geochemistry* 30: 1323–1337.
- Arouri, K. R., P. F. Greenwood, and M. R. Walter. 2000. "Biological Affinities of Neoproterozoic Acritarchs From Australia: Microscopic and Chemical Characterisation." *Organic Geochemistry* 31: 75–89.
- Baludikay, B. K., C. François, M. C. Sforza, et al. 2018. "Raman Microspectroscopy, Bitumen Reflectance and Illite Crystallinity Scale: Comparison of Different Geothermometry Methods on Fossiliferous Proterozoic Sedimentary Basins (DR Congo, Mauritania and Australia)." *International Journal of Coal Geology* 191: 80–94.
- Barker, C. E., and M. J. Pawlewicz. 1994. "Calculation of Vitrinite Reflectance From Thermal Histories and Peak Temperatures." In *Vitrinite Reflectance as a Maturity Parameter, ACS Symposium Series*, 216–229. Washington, DC, USA: American Chemical Society.
- Bartley, J. K. 1996. "Actualistic Taphonomy of Cyanobacteria: Implications for the Precambrian Fossil Record." *PALAIOS* 11: 571–586.
- Baulina, O. I. 2012. *Ultrastructural Plasticity of Cyanobacteria*. Berlin, Heidelberg, Germany: Springer-Verlag.
- Benning, L. G., V. R. Phoenix, B. W. Mountain, and H. Lappin-Scott. 2005. "Biosilicification: The Role of Cyanobacteria in Silica Sinter Deposition." In *Micro-Organisms and Earth Systems—Advances in Geomicrobiology*, edited by G. Gadd and K. Semple, 131–150. Cambridge, UK: Cambridge University Press.
- Bercovici, A., A. Hadley, and U. Villanueva-Amadoz. 2009. "Improving Depth of Field Resolution for Palynological Photomicrography." *Palaeontologia Electronica* 12: 5T.
- Berliner, M. D., D. Neely-Fisher, B. H. Rosen, and R. W. Fisher. 1987. "Spheroplast Induction in *Anabaena Variabilis* Kütz and *A. Azollae* Stras." *Protoplasma* 139: 36–40.
- Bernard, S., K. Benzerara, O. Beyssac, G. E. Brown, L. G. Stamm, and P. Düringer. 2009. "Ultrastructural and Chemical Study of Modern and Fossil Sporoderms by Scanning Transmission X-Ray Microscopy (STXM)." *Review of Palaeobotany and Palynology* 156: 248–261.
- Bernard, S., K. Benzerara, O. Beyssac, et al. 2007. "Exceptional Preservation of Fossil Plant Spores in High-Pressure Metamorphic Rocks." *Earth and Planetary Science Letters* 262: 257–272.
- Bernard, S., and B. Horsfield. 2014. "Thermal Maturation of Gas Shale Systems." *Annual Review of Earth and Planetary Sciences* 42: 635–651.
- Bernard, S., B. Horsfield, H.-M. Schulz, et al. 2010. "Multi-Scale Detection of Organic and Inorganic Signatures Provides Insights Into Gas Shale Properties and Evolution." *Chemie der Erde—Geochemistry* 70: 119–133.
- Bernard, S., B. Horsfield, H.-M. Schulz, R. Wirth, A. Schreiber, and N. Sherwood. 2012. "Geochemical Evolution of Organic-Rich Shales With Increasing Maturity: A STXM and TEM Study of the Posidonia Shale (Lower Toarcian, Northern Germany)." *Marine and Petroleum Geology* 31: 70–89.
- Beyssac, O., B. Goffé, J.-P. Petitot, E. Froigneux, M. Moreau, and J.-N. Rouzaud. 2003. "On the Characterization of Disordered and Heterogeneous Carbonaceous Materials by Raman Spectroscopy." *Spectrochimica Acta Part A: Molecular and Biomolecular Spectroscopy* 59: 2267–2276.
- Bonneville, S., F. Delpomdor, A. Prétat, et al. 2020. "Molecular Identification of Fungi Microfossils in a Neoproterozoic Shale Rock." *Science Advances* 6: eaax7599.
- Bosak, T., D. J. G. Lahr, S. B. Pruss, F. A. Macdonald, L. Dalton, and E. Matys. 2011. "Agglutinated Tests in Post-Sturtian Cap Carbonates of Namibia and Mongolia." *Earth and Planetary Science Letters* 308: 29–40.
- Brasier, M. D., J. Antcliffe, M. Saunders, and D. Wacey. 2015. "Changing the Picture of Earth's Earliest Fossils (3.5–1.9 Ga) With New Approaches



- and New Discoveries.” *Proceedings of the National Academy of Sciences, USA* 112: 4859–4864.
- Brocks, J. J., A. J. M. Jarrett, E. Sirantoine, C. Hallmann, Y. Hoshino, and T. Liyanage. 2017. “The Rise of Algae in Cryogenian Oceans and the Emergence of Animals.” *Nature* 548: 578–581.
- Butterfield, N. J. 2001. “Paleobiology of the Late Mesoproterozoic (ca. 1200 Ma) Hunting Formation, Somerset Island, Arctic Canada.” *Precambrian Research* 111: 235–256.
- Campbell, K. A., B. Y. Lynne, K. M. Handley, et al. 2015. “Tracing Biosignature Preservation of Geothermally Silicified Microbial Textures Into the Geological Record.” *Astrobiology* 15: 858–882.
- Chalansonnet, S., C. Largeau, E. Casadevall, C. Berkaloﬀ, G. Peniguel, and R. Couderc. 1988. “Cyanobacterial Resistant Biopolymers. Geochemical Implications of the Properties of Schizothrix sp. Resistant Material.” *Organic Geochemistry* 13: 1003–1010.
- Clark, R. L., and T. E. Jensen. 1969. “Ultrastructure of Akinete Development in a Blue-Green Alga, *Cylindrospermum* Sp.” *Cytologia* 34: 439–448.
- Cohen, P. A., S. W. Irvine, and J. V. Strauss. 2017. “Vase-Shaped Microfossils From the Tonian Callison Lake Formation of Yukon, Canada: Taxonomy, Taphonomy and Stratigraphic Palaeobiology.” *Palaeontology* 60: 683–701.
- Costerton, J. W., R. T. Irvin, and K. J. Cheng. 1981. “The Bacterial Glycocalyx in Nature and Disease.” *Annual Review of Microbiology* 35: 299–324.
- Coutant, M., K. Lepot, A. Fadel, et al. 2022. “Distinguishing Cellular From Abiotic Spheroidal Microstructures in the ca. 3.4 Ga Strelley Pool Formation.” *Geobiology* 20: 599–622.
- Daft, M. J., and W. D. P. Stewart. 1973. “Light and Electron Microscope Observations on Algal Lysis by Bacterium cp-i.” *New Phytologist* 72: 799–808.
- Delarue, F., J.-N. Rouzaud, S. Derenne, et al. 2016. “The Raman-Derived Carbonization Continuum: A Tool to Select the Best Preserved Molecular Structures in Archean Kerogens.” *Astrobiology* 16: 407–417.
- Demoulin, C. F., Y. J. Lara, A. Lambion, and E. J. Javaux. 2024a. “Oldest Thylakoids in Fossil Cells Directly Evidence Oxygenic Photosynthesis.” *Nature* 625: 529–534.
- Demoulin, C. F., M. C. Sforza, Y. J. Lara, et al. 2024b. “Polysphaeroides Filiformis, a Proterozoic Cyanobacterial Microfossil and Implications for Cyanobacteria Evolution.” *iScience* 27: 108865.
- Domozych, D. S. 2011. “Algal Cell Walls.” In *eLS*. Chichester, UK: John Wiley & Sons, Ltd.
- Domozych, D. S., B. Wells, and P. J. Shaw. 1992. “The Cell Wall of the Chlamydomonad Flagellate, *Gloeomonas Kupfferi* (Volvocales, Chlorophyta).” *Protoplasma* 168: 95–105.
- Fadel, A., K. Lepot, V. Busigny, A. Addad, and D. Troadec. 2017. “Iron Mineralization and Taphonomy of Microfossils of the 2.45–2.21 Ga Turee Creek Group, Western Australia.” *Precambrian Research* 298: 530–551.
- Fadel, A., K. Lepot, N. Nuns, S. Regnier, and A. Riboulleau. 2020. “New Preparation Techniques for Molecular and In-Situ Analysis of Ancient Organic Micro- and Nanostructures.” *Geobiology* 18: 445–461.
- Fairchild, I. J., A. H. Knoll, and K. Swett. 1991. “Coastal Lithofacies and Biofacies Associated With Syndepositional Dolomitization and Silicification (Draken Formation, Upper Riphean, Svalbard).” *Precambrian Research* 53: 165–197.
- Foucher, F., and F. Westall. 2013. “Raman Imaging of Metastable Opal in Carbonaceous Microfossils of the 700–800 Ma Old Draken Formation.” *Astrobiology* 13: 57–67.
- Gee, D. G., and L. M. Page. 1994. “Caledonian Terrane Assembly on Svalbard; New Evidence From 40 Ar/39 Ar Dating in Ny Friesland.” *American Journal of Science* 294: 1166–1186.
- Geitler, L. 1932. *Cyanophyceae: von Lothar Geitler*. Leipzig, Germany: Akademische Verlagsgesellschaft m.b.h.
- Golubic, S., and H. J. Hofmann. 1976. “Comparison of Holocene and Mid-Precambrian Entophysalidaceae (Cyanophyta) in Stromatolitic Algal Mats: Cell Division and Degradation.” *Journal of Paleontology* 50: 1074–1082.
- Golubić, S., and E. S. Barghoorn. 1977. “Interpretation of Microbial Fossils With Special Reference to the Precambrian.” In *Fossil Algae*, edited by E. Flügel, 1–14. Berlin, Heidelberg, Germany: Springer.
- Gomes, M. L., D. A. Fike, K. D. Bergmann, C. Jones, and A. H. Knoll. 2018. “Environmental Insights From High-Resolution (SIMS) Sulfur Isotope Analyses of Sulfides in Proterozoic Microbialites With Diverse Mat Textures.” *Geobiology* 16: 17–34.
- Gomes, M. L., L. A. Riedman, S. O’Reilly, et al. 2020. “Taphonomy of Biosignatures in Microbial Mats on Little Ambergis Cay, Turks and Caicos Islands.” *Frontiers in Earth Science* 8: 576712.
- Gong, J., K. D. Myers, C. Munoz-Saez, et al. 2020. “Formation and Preservation of Microbial Palisade Fabric In Silica Deposits From El Tatio, Chile.” *Astrobiology* 20: 500–524.
- Gonzalez-Esquer, C. R., J. Smarda, R. Rippka, et al. 2016. “Cyanobacterial Ultrastructure in Light of Genomic Sequence Data.” *Photosynthesis Research* 129: 147–157.
- Green, J. W., A. H. Knoll, S. Golubic, and K. Swett. 1987. “Paleobiology of Distinctive Benthic Microfossils from the Upper Proterozoic Limestone-Dolomite “Series,” Central East Greenland.” *American Journal of Botany* 74: 928–940.
- Guo, Z., X. Peng, A. D. Czaja, S. Chen, and K. Ta. 2018. “Cellular Taphonomy of Well-Preserved Gaoyuzhuang Microfossils: A Window Into the Preservation of Ancient Cyanobacteria.” *Precambrian Research* 304: 88–98.
- Halverson, G. P., M. Kunzmann, J. V. Strauss, and A. C. Maloof. 2018. “The Tonian-Cryogenian Transition in Northeastern Svalbard.” *Precambrian Research* 319: 79–95.
- Halverson, G. P., A. C. Maloof, D. P. Schrag, F. Ö. Dudás, and M. Hurtgen. 2007. “Stratigraphy and Geochemistry of a ca 800 Ma Negative Carbon Isotope Interval in Northeastern Svalbard.” *Chemical Geology* 237: 5–27.
- Harland, W. B., and R. A. Gayer. 1972. “The Arctic Caledonides and Earlier Oceans.” *Geological Magazine* 109: 289–314.
- Harland, W. B., R. A. Scott, K. A. Auckland, and I. Snape. 1992. “The Ny Friesland Orogen, Spitsbergen.” *Geological Magazine* 129: 679–707.
- Harland, W. B., and C. B. Wilson. 1956. “The Hecla Hoek Succession in Ny Friesland, Spitsbergen.” *Geological Magazine* 93: 265–286.
- Hendry, J. P., M. Wilkinson, A. E. Fallick, and R. S. Haszeldine. 2000. “Ankerite Cementation in Deeply Buried Jurassic Sandstone Reservoirs of the Central North Sea.” *Journal of Sedimentary Research* 70: 227–239.
- Herdianita, N. R., P. R. L. Browne, K. A. Rodgers, and K. A. Campbell. 2000. “Mineralogical and Textural Changes Accompanying Ageing of Silica Sinter.” *Mineralium Deposita* 35: 48–62.
- Hitchcock, A. P. 2023. “Analysis of X-Ray Images and Spectra (aXis2000): A Toolkit for the Analysis of X-Ray Spectromicroscopy Data.” *Journal of Electron Spectroscopy and Related Phenomena* 266: 147360.
- Hoiczky, E., and W. Baumeister. 1995. “Envelope Structure of Four Gliding Filamentous Cyanobacteria.” *Journal of Bacteriology* 177: 2387–2395.
- Hoiczky, E., and A. Hansel. 2000. “Cyanobacterial Cell Walls: News From an Unusual Prokaryotic Envelope.” *Journal of Bacteriology* 182: 1191–1199.

- Igisu, M., Y. Ueno, M. Shimojima, et al. 2009. "Micro-FTIR Spectroscopic Signatures of Bacterial Lipids in Proterozoic Microfossils." *Precambrian Research* 173: 19–26.
- Jakubek, R. S., and M. D. Fries. 2023. "Laser Raman Induced Degradation of Macromolecular Carbon in Coals and Meteorites." *Earth and Space Science* 10: e2022EA002724.
- Javaux, E. J., A. H. Knoll, and M. R. Walter. 2003. "Recognizing and Interpreting the Fossils of Early Eukaryotes." *Origins of Life and Evolution of the Biosphere* 33: 75–94.
- Javaux, E. J., A. H. Knoll, and M. R. Walter. 2004. "TEM Evidence for Eukaryotic Diversity in Mid-Proterozoic Oceans." *Geobiology* 2: 121–132.
- Javaux, E. J., and K. Lepot. 2018. "The Paleoproterozoic Fossil Record: Implications for the Evolution of the Biosphere During Earth's Middle-Age." *Earth-Science Reviews* 176: 68–86.
- Jones, B., R. W. Renaut, and M. R. Rosen. 1998. "Microbial Biofacies in Hot-Spring Sinters: A Model Based on Ohaaki Pool, North Island, New Zealand." *Journal of Sedimentary Research* 68: 413–434.
- Jones, B., R. W. Renaut, and M. R. Rosen. 2001. "Taphonomy of Silicified Filamentous Microbes in Modern Geothermal Sinters—Implications for Identification." *PALAIOS* 16: 580–592.
- Katz, B. J., and I. Arango. 2018. "Organic Porosity: A geochemist's View of the Current State of Understanding." *Organic Geochemistry* 123: 1–16.
- Kaznatcheev, K. V., C. Karunakaran, U. D. Lanke, S. G. Urquhart, M. Obst, and A. P. Hitchcock. 2007. "Soft X-Ray Spectromicroscopy Beamline at the CLS: Commissioning Results." *Nuclear Instruments and Methods in Physics Research Section A: Accelerators, Spectrometers, Detectors and Associated Equipment* 582: 96–99.
- Kempe, A., R. Wirth, W. Altermann, R. W. Stark, J. W. Schopf, and W. A. Heckl. 2005. "Focussed Ion Beam Preparation and In Situ Nanoscopic Study of Precambrian Acritarchs." *Precambrian Research* 140: 36–54.
- Knoll, A. H. 1982. "Microorganisms From the Late Precambrian Draken Conglomerate, Ny Friesland, Spitsbergen." *Journal of Paleontology* 56: 755–790.
- Knoll, A. H. 1985. "Exceptional Preservation of Photosynthetic Organisms in Silicified Carbonates and Silicified Peats." *Philosophical Transactions of the Royal Society of London B, Biological Sciences* 311: 111–122.
- Knoll, A. H. 2003. "Life's Signature in Ancient Rocks." In *Life on a Young Planet: The First Three Billion Years of Evolution on Earth*. Edited by L. Packer, A. N. Glazer. Princeton, NJ, USA: Princeton University Press.
- Knoll, A. H., and E. S. Barghoorn. 1975. "Precambrian Eukaryotic Organisms: A Reassessment of the Evidence." *Science* 190: 52–54.
- Knoll, A. H., K. D. Bergmann, and J. V. Strauss. 2016. "Life: The First Two Billion Years." *Philosophical Transactions of the Royal Society, B: Biological Sciences* 371: 20150493.
- Knoll, A. H., and S. Golubic. 1979. "Anatomy and Taphonomy of a Precambrian Algal Stromatolite." *Precambrian Research* 10: 115–151.
- Knoll, A. H., P. Strother, and S. Rossi. 1988. "Distribution and Diagenesis of Microfossils From the Lower Proterozoic Duck Creek Dolomite, Western Australia." *Precambrian Research* 38: 257–279.
- Knoll, A. H., K. Sweet, and J. Mark. 1991. "Paleobiology of a Neoproterozoic Tidal Flat/Lagoonal Complex: The Draken Conglomerate Formation, Spitsbergen." *Journal of Paleontology* 65: 531–570.
- Knoll, A. H., and K. Swett. 1990. "Carbonate Deposition During the Late Proterozoic Era: An Example From Spitsbergen." *American Journal of Science* 290-A: 104–132.
- Koehler, I., K. O. Konhauser, D. Papineau, A. Bekker, and A. Kappler. 2013. "Biological Carbon Precursor to Diagenetic Siderite With Spherical Structures in Iron Formations." *Nature Communications* 4: 1741.
- Konhauser, K. O., B. Jones, V. Phoenix, G. Ferris, and R. Renaut. 2004. "The Microbial Role in Hot Spring Silicification." *Ambio* 33: 552–558.
- Kouketsu, Y., T. Mizukami, H. Mori, et al. 2014. "A New Approach to Develop the Raman Carbonaceous Material Geothermometer for Low-Grade Metamorphism Using Peak Width: Raman CM Geothermometer Using FWHM." *Island Arc* 23: 33–50.
- Lahfid, A., O. Beyssac, E. Deville, F. Negro, C. Chopin, and B. Goffé. 2010. "Evolution of the Raman Spectrum of Carbonaceous Material in Low-Grade Metasediments of the Glarus Alps (Switzerland): RSCM in Low-Grade Metasediments." *Terra Nova* 22: 354–360.
- Lalonde, S. V., K. O. Konhauser, A.-L. Reysenbach, and F. G. Ferris. 2005. "The Experimental Silicification of Aquificales and Their Role in Hot Spring Sinter Formation." *Geobiology* 3: 41–52.
- Lang, N. J. 1968. "The Fine Structure of Blue-Green Algae." *Annual Review of Microbiology* 22: 15–46.
- Le Guillou, C., S. Bernard, F. De la Pena, and Y. Le Brech. 2018. "XANES-Based Quantification of Carbon Functional Group Concentrations." *Analytical Chemistry* 90: 8379–8386.
- Lekele Baghekema, S. G., K. Lepot, A. Riboulleau, A. Fadel, A. Trentesaux, and A. El Albani. 2017. "Nanoscale Analysis of Preservation of Ca. 2.1 Ga Old Francevillian Microfossils, Gabon." *Precambrian Research* 301: 1–18.
- Lemelle, L., P. Labrot, M. Salome, A. Simionovici, M. Viso, and F. Westall. 2008. "In Situ Imaging of Organic Sulfur in 700–800 My-Old Neoproterozoic Microfossils Using X-Ray Spectromicroscopy at the SK-Edge." *Organic Geochemistry* 39: 188–202.
- Lepot, K. 2020. "Signatures of Early Microbial Life From the Archean (4 to 2.5 Ga) eon." *Earth-Science Reviews* 209: 103296.
- Lepot, K. 2021. "Microfossils, Analytical Techniques." In *Encyclopedia of Astrobiology*, edited by M. Gargaud, W. M. Irvine, R. Amils, H. J. Cleaves, D. Pinti, J. Cernicharo Quintanilla, and M. Viso, 1–16. Berlin, Heidelberg, Germany: Springer.
- Lepot, K., A. Addad, A. H. Knoll, et al. 2017. "Iron Minerals Within Specific Microfossil Morphospecies of the 1.88 Ga Gunflint Formation." *Nature Communications* 8: 1–11.
- Lepot, K., K. Benzerara, G. E. Brown, and P. Philippot. 2008. "Microbially Influenced Formation of 2,724-Million-Year-Old Stromatolites." *Nature Geoscience* 1: 118–121.
- Lepot, K., P. Compere, E. Gerard, et al. 2014. "Organic and Mineral Imprints in Fossil Photosynthetic Mats of an East Antarctic Lake." *Geobiology* 12: 424–450.
- Liberton, M., R. Howard Berg, J. Heuser, R. Roth, and H. B. Pakrasi. 2006. "Ultrastructure of the Membrane Systems in the Unicellular Cyanobacterium *Synechocystis* sp. Strain PCC 6803." *Protoplasma* 227: 129–138.
- Liu, D., X. Xiao, H. Tian, et al. 2013. "Sample Maturation Calculated Using Raman Spectroscopic Parameters for Solid Organics: Methodology and Geological Applications." *Chinese Science Bulletin* 58: 1285–1298.
- Liu, Y., H. E. King, M. A. Van Huis, M. R. Drury, and O. Plümper. 2016. "Nano-Tomography of Porous Geological Materials Using Focused Ion Beam-Scanning Electron Microscopy." *Minerals* 6: 104.
- Lyberis, N., and G. Manby. 1999. "Continental Collision and Lateral Escape Deformation in the Lower and Upper Crust: An Example From Caledonide Svalbard." *Tectonics* 18: 40–63.



- Lynne, B. Y., K. A. Campbell, J. N. Moore, and P. R. L. Browne. 2005. "Diagenesis of 1900-Year-Old Siliceous Sinter (Opal-A to Quartz) at Opal Mound, Roosevelt Hot Springs, Utah, USA." *Sedimentary Geology* 179: 249–278.
- Maloof, A. C., G. P. Halverson, J. L. Kirschvink, D. P. Schrag, B. P. Weiss, and P. F. Hoffman. 2006. "Combined Paleomagnetic, Isotopic, and Stratigraphic Evidence for True Polar Wander From the Neoproterozoic Akademikerbreen Group, Svalbard, Norway." *GSA Bulletin* 118: 1099–1124.
- Manning-Berg, A. R., R. S. Wood, K. H. Williford, A. D. Czaja, and L. C. Kah. 2019. "The Taphonomy of Proterozoic Microbial Mats and Implications for Early Diagenetic Silicification." *Geosciences* 9: 40.
- Mareš, J., O. Strunecký, L. Bučinská, and J. Wiedermannová. 2019. "Evolutionary Patterns of Thylakoid Architecture in Cyanobacteria." *Frontiers in Microbiology* 10: 434–523.
- Martí Mus, M., M. Moczydłowska, and A. H. Knoll. 2020. "Morphologically Diverse Vase-Shaped Microfossils From the Russoya Member, Elbobreen Formation, in Spitsbergen." *Precambrian Research* 350: 105899.
- Miller, M. M., and N. J. Lang. 1968. "The Fine Structure of Akinete Formation and Germination in *Cylindrospermum*." *Archiv für Mikrobiologie* 60: 303–313.
- Moczydłowska, M. 2011. "The Early Cambrian Phytoplankton Radiation: Acritarch Evidence From the Lükati Formation, Estonia." *Palynology* 35: 103–145.
- Moczydłowska, M., and S. Willman. 2009. "Ultrastructure of Cell Walls in Ancient Microfossils as a Proxy to Their Biological Affinities." *Precambrian Research* 173: 27–38.
- Morais, L., D. J. G. Lahr, I. D. Rudnitzki, et al. 2019. "Insights Into Vase-Shaped Microfossil Diversity and Neoproterozoic Biostratigraphy in Light of Recent Brazilian Discoveries." *Journal of Paleontology* 93: 612–627.
- Mühlsteinová, R., T. Hauer, P. De Ley, and N. Pietrasiak. 2018. "Seeking the True Oscillatoria: A Quest for a Reliable Phylogenetic and Taxonomic Reference Point." *Preslia* 90: 151–169.
- Nabhan, S., L. C. Kah, B. Mishra, K. Pollok, A. R. Manning-Berg, and M. A. van Zuilen. 2021. "Structural and Chemical Heterogeneity of Proterozoic Organic Microfossils of the ca. 1 Ga Old Angmaat Formation, Baffin Island, Canada." *Geobiology* 19: 557–584.
- Nims, C., J. Lafond, J. Alleon, A. S. Templeton, and J. Cosmidis. 2021. "Organic Biomorphs May Be Better Preserved Than Microorganisms in Early Earth Sediments." *Geology* 49: 629–634.
- Oehler, D. Z. 1976a. "Transmission Electron Microscopy of Organic Microfossils From the Late Precambrian Bitter Springs Formation of Australia: Techniques and Survey of Preserved Ultrastructure." *Journal of Paleontology* 50: 90–106.
- Oehler, D. Z. 1977. "Pyrenoid-Like Structures in Late Precambrian Algae From the Bitter Springs Formation of Australia." *Journal of Paleontology* 51: 885–901.
- Oehler, D. Z., F. Robert, S. Mostefaoui, A. Meibom, M. Selo, and D. S. McKay. 2006. "Chemical Mapping of Proterozoic Organic Matter at Submicron Spatial Resolution." *Astrobiology* 6: 838–850.
- Oehler, J. H. 1976b. "Hydrothermal Crystallization of Silica-Gel." *Geological Society of America Bulletin* 87: 1143–1152.
- Orange, F., F. Westall, J.-R. Disnar, et al. 2009. "Experimental Silicification of the Extremophilic Archaea *Pyrococcus abyssi* and *Methanocaldococcus jannaschii*: Applications in the Search for Evidence of Life in Early Earth and Extraterrestrial Rocks." *Geobiology* 7: 403–418.
- Pacton, M., G. E. Gorin, and N. Fiet. 2008. "Unravelling the Origin of Ultralaminae in Sedimentary Organic Matter: The Contribution of Bacteria and Photosynthetic Organisms." *Journal of Sedimentary Research* 78: 654–667.
- Phoenix, V. R., D. G. Adams, and K. O. Konhauser. 2000. "Cyanobacterial Viability During Hydrothermal Biomineralisation." *Chemical Geology* 169: 329–338.
- Porter, S. M., and A. H. Knoll. 2000. "Testate Amoebae in the Neoproterozoic Era: Evidence From Vase-Shaped Microfossils in the Chuar Group, Grand Canyon." *Paleobiology* 26: 360–385.
- Porter, S. M., R. Meisterfeld, and A. H. Knoll. 2003. "Vase-Shaped Microfossils From the Neoproterozoic Chuar Group, Grand Canyon: A Classification Guided by Modern Testate Amoebae." *Journal of Paleontology* 77: 409–429.
- Posth, N. R., I. Koehler, E. D. Swanner, et al. 2013. "Simulating Precambrian Banded Iron Formation Diagenesis." *Chemical Geology* 362: 66–73.
- Preston, L. J., G. K. Benedix, M. J. Genge, and M. A. Sephton. 2008. "A Multidisciplinary Study of Silica Sinter Deposits With Applications to Silica Identification and Detection of Fossil Life on Mars." *Icarus* 198: 331–350.
- Rasmussen, B., and J. R. Muhling. 2019. "Organic-Rich Microfossils Produced by Oil Infiltration of Hollow Silicified Bacteria: Evidence From the ca. 340 Ma Red Dog Zn-Pb Deposit, Alaska." *Geology* 47: 1107–1111.
- Rasmussen, B., J. R. Muhling, and W. W. Fischer. 2021. "Ancient Oil as a Source of Carbonaceous Matter in 1.88-Billion-Year-Old Gunflint Stromatolites and Microfossils." *Astrobiology* 21: 655–672.
- Riedman, L. A., S. M. Porter, and C. R. Calver. 2018. "Vase-Shaped Microfossil Biostratigraphy With New Data From Tasmania, Svalbard, Greenland, Sweden and the Yukon." *Precambrian Research* 319: 19–36.
- Sasaki, K., A. Ishida, N. Takahata, Y. Sano, and T. Kakegawa. 2022. "Evolutionary Diversification of Paleoproterozoic Prokaryotes: New Microfossil Records in 1.88 Ga Gunflint Formation." *Precambrian Research* 380: 106798.
- Schiffbauer, J. D., and S. Xiao. 2009. "Novel Application of Focused Ion Beam Electron Microscopy (FIB-EM) in Preparation and Analysis of Microfossil Ultrastructures: A New View of Complexity in Early Eukaryotic Organisms." *PALAIOS* 24: 616–626.
- Schopf, J. W. 1968. "Microflora of the Bitter Springs Formation, Late Precambrian, Central Australia." *Journal of Paleontology* 42: 651–688.
- Schopf, J. W. 1970. "Electron Microscopy of Organically Preserved Precambrian Microorganisms." *Journal of Paleontology* 44: 1–6.
- Schopf, J. W., and A. B. Kudryavtsev. 2009. "Confocal Laser Scanning Microscopy and Raman Imagery of Ancient Microscopic Fossils." *Precambrian Research* 173: 39–49.
- Schopf, J. W., A. B. Kudryavtsev, D. G. Agresti, A. D. Czaja, and T. J. Wdowiak. 2005. "Raman Imagery: A New Approach to Assess the Geochemical Maturity and Biogenicity of Permineralized Precambrian Fossils." *Astrobiology* 5: 333–371.
- Stanier (Cohen-Bazire), G. 1988. "[14] Fine Structure of Cyanobacteria." In *Methods in Enzymology, Cyanobacteria*, edited by L. Packer and A. N. Glazer, 157–172. Cambridge, MA, USA: Academic Press.
- Steele, A., L. G. Benning, R. Wirth, et al. 2022. "Organic Synthesis Associated With Serpentinization and Carbonation on Early Mars." *Science* 375: 172–177.
- Strauss, J. V., A. D. Rooney, F. A. Macdonald, A. D. Brandon, and A. H. Knoll. 2014. "740 Ma Vase-Shaped Microfossils From Yukon, Canada: Implications for Neoproterozoic Chronology and Biostratigraphy." *Geology* 42: 659–662.
- Tang, Q., K. Pang, X. Yuan, and S. Xiao. 2020. "A One-Billion-Year-Old Multicellular Chlorophyte." *Nature Ecology & Evolution* 4: 543–549.

- van de Meene, A. M. L., M. F. Hohmann-Marriott, W. F. J. Vermaas, and R. W. Roberson. 2006. "The Three-Dimensional Structure of the Cyanobacterium *Synechocystis* sp. PCC 6803." *Archives of Microbiology* 184: 259–270.
- Versteegh, G. J. M., P. Blokker, G. D. Wood, M. E. Collinson, J. S. Sinninghe Damsté, and J. W. Leeuw. 2004. "An Example of Oxidative Polymerization of Unsaturated Fatty Acids as a Preservation Pathway for Dinoflagellate Organic Matter." *Organic Geochemistry* 35: 1129–1139.
- Wacey, D., K. Eiloart, and M. Saunders. 2019a. "Comparative Multi-Scale Analysis of Filamentous Microfossils From the c. 850Ma Bitter Springs Group and Filaments From the c. 3460Ma Apex Chert." *Journal of the Geological Society* 176: 1247–1260.
- Wacey, D., N. McLoughlin, M. R. Kilburn, et al. 2013. "Nanoscale Analysis of Pyritized Microfossils Reveals Differential Heterotrophic Consumption in the ~1.9-Ga Gunflint Chert." *Proceedings of the National Academy of Sciences of the United States of America* 110: 8020–8024.
- Wacey, D., S. Menon, L. Green, et al. 2012. "Taphonomy of Very Ancient Microfossils From the Similar to 3400 ma Strelley Pool Formation and Similar to 1900 Ma Gunflint Formation: New Insights Using a Focused Ion Beam." *Precambrian Research* 220: 234–250.
- Wacey, D., E. Sirantoine, M. Saunders, and P. Strother. 2019b. "1 Billion-Year-Old Cell Contents Preserved in Monazite and Xenotime." *Scientific Reports* 9: 9068.
- Waterbury, J. B., and R. Y. Stanier. 1978. "Patterns of Growth and Development in Pleurocapsalean Cyanobacteria." *Microbiological Reviews* 42: 2–44.
- Westall, F., L. Boni, and E. Guerzoni. 1995. "The Experimental Silicification of Microorganisms." *Palaeontology* 38: 495–528.
- Williford, K. H., T. Ushikubo, J. W. Schopf, K. Lepot, K. Kitajima, and J. W. Valley. 2013. "Preservation and Detection of Microstructural and Taxonomic Correlations in the Carbon Isotopic Compositions of Individual Precambrian Microfossils." *Geochimica et Cosmochimica Acta* 104: 165–182.
- Willman, S. 2009. "Morphology and Wall Ultrastructure of Leiosphaeric and Acanthomorphic Acritarchs From the Ediacaran of Australia." *Geobiology* 7: 8–20.
- Willman, S., and P. A. Cohen. 2011. "Ultrastructural Approaches to the Microfossil Record: Assessing Biological Affinities by Use of Transmission Electron Microscopy." In *Quantifying the Evolution of Early Life: Numerical Approaches to the Evaluation of Fossils and Ancient Ecosystems, Topics in Geobiology*, edited by M. Laflamme, J. D. Schiffbauer, and S. Q. Dornbos, 301–320. Dordrecht, The Netherlands: Springer Netherlands.
- Wilson, C. B. 1961. "The Upper Middle Hecla Hoek Rocks of Ny Friesland, Spitsbergen." *Geological Magazine* 98: 89–116.
- Wingate, M., I. O. H. Fielding, Y. Lu, D. M. Martin, and H. J. Allen. 2022. "242931: volcanoclastic siltstone, Mount Berry." *Geochronology Record* 1898: Geological Survey of Western Australia 4p.
- Wojdyr, M. 2010. "Fityk: A General-Purpose Peak Fitting Program." *Journal of Applied Crystallography* 43: 1126–1128.
- Zhang, T., C. B. Keller, M. J. Hoggard, et al. 2023. "A Bayesian Framework for Subsidence Modeling in Sedimentary Basins: A Case Study of the Tonian Akademikerbreen Group of Svalbard, Norway." *Earth and Planetary Science Letters* 620: 118317.
- Zhang, Y. 1981. "Proterozoic Stromatolite Microfloras of the Gaoyuzhuang Formation (Early Sinian: Riphean), Hebei, China." *Journal of Paleontology* 55: 485–506.
- Zheng, W., U. Rasmussen, S. Zheng, et al. 2013. "Multiple Modes of Cell Death Discovered in a Prokaryotic (Cyanobacterial) Endosymbiont." *PLoS One* 8: e66147.

## Supporting Information

Additional supporting information can be found online in the Supporting Information section.